AIMS Mathematics

http://www.aimspress.com/journal/Math

AIMS Mathematics, 6(6): 5942–5976.
DOI: 10.3934/math.2021352
Received: 19 January 2021
Accepted: 08 March 2021
Published: 30 March 2021

Research article

Analysis and modeling of fractional electro-osmotic ramped flow of chemically reactive and heat absorptive/generative Walters' B fluid with ramped heat and mass transfer rates

Asifa[1], Poom Kumam[2,3,5,*], Talha Anwar[1], Zahir Shah[4,5] and Wiboonsak Watthayu[1]

[1] Department of Mathematics, Faculty of Science, King Mongkut's University of Technology Thonburi, 126 Pracha-Uthit Road, Bang Mod, Thung Khru, Bangkok 10140, Thailand

[2] KMUTT Fixed Point Research Laboratory, SCL 802 Fixed Point Laboratory, Science Laboratory Building, Department of Mathematics, Faculty of Science, King Mongkut's University of Technology Thonburi (KMUTT), Bangkok 10140, Thailand

[3] Department of Medical Research, China Medical University Hospital, China Medical University, Taichung 40402, Taiwan

[4] Department of Mathematics, University of Lakki Marwat, Lakki Marwat 28420, Khyber Pakhtunkhwa Pakistan

[5] Center of Excellence in Theoretical and Computational Science (TaCS-CoE), Science Laboratory Building, Faculty of Science, King Mongkut's University of Technology Thonburi (KMUTT), 126 Pracha-Uthit Road, Bang Mod, Thung Khru, Bangkok 10140, Thailand

* **Correspondence:** Email: poom.kum@kmutt.ac.th.

Abstract: In this contemporary era, fractional derivatives are widely used for the development of mathematical models to precisely describe the dynamics of real-world physical processes. In the field of fluid mechanics, analysis of thermal performance and flow behavior of non-Newtonian fluids is a topic of interest for a variety of researchers due to their significant applications in several industries, engineering operations, devices, and thermal equipment. The primary focus of this article is to investigate the effectiveness of jointly imposed time-controlled (ramped) boundary conditions in the electro-osmotic flow of a chemically reactive and radiative Walters' B fluid along with concentration and energy distributions. In Particular, the concept of using piece-wise time-dependent mass, motion, and energy conditions simultaneously for any non-Newtonian fluid is extensively explored in this work. The flow is developed due to the motion of the bounding vertical wall, which is suspended in a porous material subject to heat injection/absorption and uniform magnetic influences. Atangana-Baleanu derivative of order ψ is incorporated to establish the fractional form of ordinary modeled equations. Laplace transform method is adapted in light of some unit-less quantities to procure the exact solutions of the under observation model. Several graphical delineations are

produced to comprehensively analyze the key characteristics of many physical and thermal parameters. To highlight the significance of operating surface conditions, solutions are compared for time-dependent and constant boundary conditions in every graph. Furthermore, the role of the fractional parameter, time-dependent conditions, and different other involved parameters in heat transfer, mass transfer, and flow rates is characterized by determining the expressions for Nusselt and Sherwood number and coefficient of skin friction. The numerical outcomes are organized in several tables to deeply scrutinize the noteworthy variations in the behavior of the aforementioned physical quantities. The graphical study reveals that the parameter E_s accounting for electro-osmotic effects decelerates the flow of fluid. At the atomic level, such electro-osmotic flows are useful in the separation processes of the liquids. The fractional parameter ψ attenuates thicknesses of boundary layers for the evolution of time t but, it exhibits an opposite role for smaller values of t. It is also noted that the direct correspondence between velocity and time at the boundary for time duration $t < 1$ plays a supportive part to effectively control the flow. The exercise tolerance level of cardiac patients is anticipated by following a ramped velocity based protocol. The fractional models are more effective than ordinary models for restricting the boundary shear stress. The occurrence of a chemical reaction leads to improving the mass transfer rate. Additionally, augmentation in heat transfer rate due to the ramped heating technique indicates the significance of this technique in cooling processes. The findings of this work are helpful for clear and comprehensive understanding of electro-osmotic flow of Walters' B fluid in a fractional framework together with chemically reacted mass transfer and thermally radiative heat transfer phenomena subject to wall ramping technique.

Keywords: ramped heat transfer; electro-osmotic flow; porous media; Laplace transform; chemical reaction; heat absorption/generation
Mathematics Subject Classification: 26A33, 35R11, 76D05

Nomenclature

t'	Time
g	Acceleration due to gravity
y'	Spatial variable
u'	Velocity component
M_0	Applied magnetic field
D	mass diffusion
t'_0	Characteristic time
R'	Rate of chemical reaction
Q_1	Thermal injection/absorption coefficient
Q_r	Thermal radiative flux
E_x	External electric field
C_p	Specific heat capacitance
t	Unit-less time
W_f	Unit-less parameter of Walters' B fluid
E_s	Electro-osmotic parameter
Gr_1	Thermal Grashof number

Gr_2	Mass Grashof number
Pr	Prandtl number
R	Radiation parameter
M	Magnetic parameter
Q	Heat injection/absorption parameter
Sc	Schmidt number
K	Permeability parameter
C_R	Chemical reaction parameter
p	Laplace parameter

Greek symbols

ρ	Fluid density
β_1	Coefficient of thermal expansion
β_2	Coefficient of mass expansion
Θ'	Fluid temperature
Φ'	Fluid concentration
μ	Dynamic viscosity
ρ_e	Total charge density
ϵ	Permeability of the fluid
ψ_w	Induced electrical potential
κ_0, α_0	Walters' B fluid parameters
σ	Electric conductance
κ_1	Permeability of the medium
κ_2	Thermal conductance
$\mathfrak{J}'_0$	Characteristic velocity
ν	Kinematic viscosity
Θ'_w	Wall temperature
Φ'_w	Wall concentration
φ	Porosity parameter
Θ'_∞	Ambient temperature
Φ'_∞	Ambient concentration
ϵ_r	Stefan-Boltzmann constant
κ_r	Coefficient of Rosseland absorption
ζ	Unit-less axial variable
Ψ	Unit-less fluid velocity
Θ	Unit-less fluid temperature
Φ	Unit-less fluid concentration

1. Introduction

In modern times, electro-osmosis is a preeminent and stimulating mechanism due to its involvement in several kinds of devices at macro and nano scales. An abundant range of its practical applications includes bio-pharmaceutical inspections, industrial operations, chemical separation

procedures, and biochemistry. The migration of a liquid caused due to the imposition of electric power about mediums with porous holes, blood vessels, micro-channels, layers of cells, or any other fluid conveying systems is termed as electro-osmosis. The credit for this electrifying mechanism is attributed to Reuss [1]. In the initial decade of 19^{th} century, he introduced the idea of electro-osmosis on water transportation through clay during his pioneering experimental research. About four decades later, following the theme of Reuss, Wiedemann [2] reconfigured the experiment and discussed the formal mathematics involved in this phenomenon. Mainly, electro-osmotic flows involve the transport of ions, and they are described with the assistance of some fundamental theories and principles. A few of them are Helmholtz-Smudchowski theory [3], Schmid's theory, Debye-Huckel approximation, and ion-hydration theory [4, 5]. In recent times, various imperative devices of microfluidics operate on the principle of electro-osmosis to achieve the rigorous delivery of the involved fluids. The exceptional role of microfluidics can be found in nanotechnology, energy harvesting, micro-propulsion, material processing, determining prognosis, and development of Deoxyribonucleic acid chips. Additionally, microfluidic flows specify some stimulating consequences and unintuitive features. For instance, there are minute chances for the traditional mixing of different fluids because, at the micro-scale, these flows become laminar. Besides this, such flows ensure the high specificity of physical and chemical characteristics, which leads to produce better reactive conditions [6]. However, the major complication faced in microfluidics is the actuation of fluid flow that is usually procured through the ability of fluid to integrate with surface-tension of conduits or due to the combined action of electrokinetic and capillary forces. The said complication arises as a consequence of size depletion of section geometry to micro-scale because, for such cases, the size of the channel strongly influences the velocity of the fluid. An adequate alternative to overcome this issue is the external pumping of fluids via peristalsis, mechanical pumps, electro-osmosis, syringe pumps, or some other exterior pressure sources. The primary reason to operate electro-osmosis as the preferred external pumping means is that the conduit measurements have no effects on the velocity of the fluid. Some supplementary advantages of electro-osmosis are accurate mobility, better control, enhanced efficiency, easily implementable, non-moving mechanical parts, and inexpensive fabrication of devices [7, 8]. Observing the broad utility range of electro-osmosis, numerous engineers and scientists are focused to explore the vast effectiveness of this phenomenon for various working liquids such as blood, polymeric arrangements, salt solutions, industrial adhesives, colloidal suspensions, and so forth. In this regard, multitudinous numerical [9–12], theoretical [13–16], and experimental [17] investigations have been performed to mature the available facts.

Keeping view of the significant relevance of electro-osmotic flows in the development of microfluidic equipment, Hadian et al. [18] adapted an analytic technique to evaluate the temperature distribution associated with electro-osmotic flow established through a slit microchannel and to find the relative contribution of imposed electric strength and channel height in development of the temperature distribution. Dejam [19] computed an analytic expression to discuss the dispersion phenomenon for the electro-osmotic flow of a viscoelastic fluid inside a channel, which possesses porous walls. Mishra and Sinha [20] considered the biological problem of heat transfer in blood carriage through an artery with Navier slip as a practical-life demonstrative example of electro-osmosis. Recently, Ponalagusamy and Manchi [21] reported that the combined application of magnetic and electric fields substantially controls Jeffrey fluid transport through a stenosed duct with blood cell dispersion. Azari et al. [22] presented analytic solutions to investigate an exclusive

coupling between heat transmission and surface charge asymmetries for an electro-osmosis flow inside a circular channel. A computational model to analyze electro-osmosis through a microfluidic porous channel subject to various flow profiles is formulated by Dejam [23]. Moghadam [24] examined the thermal efficiency of some electro-osmotically established flows in an annulus to study the influence of several alternatively appearing electric fields.

The fluids accounting mass and heat transmission phenomena at the same time are of broad utilization in several industrial and chemical engineering problems such as sample separation, temperature preservation, climate control, and food processing. Heat and mass transfer collectively take place due to the simultaneous impacts of species and energy gradients. In many complex engineering situations, the combined occurrence of these phenomena in electromagnetically established flows possesses a crucial contribution. Particularly mass transfer is considered a fundamental unit for multiple biological, aeronautical, and chemical problems. For instance, the transfer of ions inside the kidney through membranes and oxygenation of the human body are sub-disciplines of biological processes. Meanwhile, the formation of semiconducting thin films, water purification, coating of a silicon wafer, and polymer production are some common examples of chemical processes [25]. To examine the main impacts of a chemical reaction and activation energy, Khan et al. [26] derived the dual solutions for magneto cross liquid migration close to a moving wedge. Systematic research was carried out to scrutinize the mass transfer mechanism of magnetohydrodynamic (MHD) Casson fluid under variable energy and solutal surface constraints by Kataria and Patel [27]. Zhao [28] operated a hybrid numerical method to explore the consequences of species diffusion on the free convectional transport of an Oldroyd-B nanofluid. Moving forward, it is worth considering that the heat transmission process can be maneuvered through radiation and induction of some heat injector/absorbent to achieve the desired result. The applications of radiative flows are witnessed at various industrial and environmental stages. For example, water evaporation from open channels, cooling and heating chambers, nuclear plants, combustion, and astrophysical flows [29]. Likewise, the installation of a heat injector/absorbent is an efficient solution for several complex problems like cooling of chips, heat treatments, ventilation, better performance of microprocessors, and storage of foodstuff [30]. Recently proposed studies on radiative flows including injection or absorption of heat have opened many new horizons. Saeed et al. [31] discussed the Maxwell fluid migration over an extending cylinder to highlight the productivity of heat injection/absorption and radiation for convective flows. Baslem et al. [32] utilized a numerical approach to analyze the improvement in the thermal behavior of some nanofluids resulted due to radiation phenomenon. Hayat et al. [33] theoretically addressed the role of nonlinear radiative flux and heat injector/absorbent to minimize the entropy generation. The effects of radiation on thermal functioning of chemically reactive Casson fluid during mixed convective flow near an inclined surface were deliberated by Sulochana et al. [34].

The idea of fractional calculus came into existence on the basis of a query made by L'Hospital in 1965. In a letter, he inquired from Leibniz about the best practical description of the nth derivative of an arbitrary function $F(x)$ when $n = 1/2$. In modern times, it is a well-recognized fact that L'Hospital's letter was the first discussion about fractional derivatives. To achieve the differentiation cause in an efficient manner, the utilization of fractional derivatives is more effectual as equated with regular derivatives. Mainly there are two key reasons firstly, there is no restriction on the choice of fractional parametric value, which leads to produce exceptional accordance between experimental

results and theoretical information. Secondly, fractional derivatives encounter both current and previous time steps, and this characteristic makes them more adequate to restore and communicate the memory effects. Fractional derivatives have a remarkable history and a vast range of applications in multitudinous disciplines of economics, signal processing, biotechnology, medical, viscoelasticity, and many more [35–37]. Kumar et al. [38] constructed a fractional model to anticipate the expansion of malaria and to propose the medication via sprays, pills, and vaccination. Ahmed et al. [39] analyzed the principal reliability extent of lockdown to mitigate the dissemination of novel coronavirus by proposing a fractional model based on the Caputo derivative. Ullah and Khan [40] formulated a non-integer order model to evaluate the dynamics of hepatitis B and to develop the strategies for limiting the spread of the disease. Acay et al. [41] performed a comprehensive investigation to explore multiple aspects of different economical problems with the help of diverse fractional derivatives.

The development of different fractional operators is based on the convolution of classical derivatives and some particular kernels. Several kernels have been advised in the literature, which possess practical advantages on each other coupled with particular limitations. For example, the differentiation of a constant value is not zero in the case of the operator proposed by Reiman and Liouville [42]. Caputo [43] eliminated this limitation by proposing a different fractional operator, which later encountered the observations of having a singular kernel. To address the marked fault, Caputo and Fabrizio [44] further advised a model with a special exponential kernel. After its utilization in a variety of analyses, the disadvantage of possessing a local kernel came into sight. In particular, the incapability of a local kernel to exhibit the memory effect is the primary concern here. Atangana and Baleanu [45] circumvented the shortcomings of the aforementioned operator by propounding a novel operator containing a unique kernel that is neither local nor singular. In fluid mechanics, there are extensive applications of fractional operators to delineate the elastic, thermal, material, and viscous properties of various fluids. Furthermore, some of the essential rheological qualities of industrial liquids are precisely anticipated only through non-integer order simulations. Gemant [46] initiated the use of fractional calculus in viscoelasticity. With the assistance of semi-analytic expressions, Aman et al. [47] explored the physical behavior of Maxwell fluid subject to second-order slip flow. Awan et al. [48] operated a non-singular kernel to scrutinize electro-osmotic slip transportation of second grade fluid contained by two parallel unbounded walls. Jiang et al. [49] analyzed the electromagnetically developed circular motion of fractional Oldroyd-B fluid by employing Hankel and Laplace transformation methods. Asjad et al. [50] constructed a model with a non-integer order to explore the thermal behavior of a chemically reactive nanofluid composed of carbon nanotubes and Carboxyl methylcellulose.

The literature review discloses that piece-wise time-dependent boundary conditions are not jointly operated for momentum, concentration, and energy equations of a non-Newtonian fluid. Particularly, there is no fractional model in terms of Atangana-Baleanu fractional derivative, which studies the flow behavior of a chemically reactive and thermally radiative Walters' B fluid under heat injection/absorption effects. Moreover, there are very few investigations that simultaneously examine electro-osmotic flows with heat transfer phenomenon. The novelty of this work is the development of a fractional model based on Atangana-Baleanu fractional derivative to study the electro-osmotic transport mechanism of Walters' B fluid together with mass and heat transfer. In addition to this, piece-wise time-dependent boundary conditions are applied at the boundary wall to establish

foregoing phenomena. The vertical wall is assumed to be nested in a porous material subject to the imposition of a magnetic influence. Laplace transform method is employed to produce integral form exact solutions of the modeled problem. These solutions are further utilized in determining the gradients of velocity, concentration, and energy functions to obtain the expressions for skin friction coefficient, Sherwood number, and Nusselt number respectively. A detailed illustrative and tabular analysis is performed to explore the quantities of physical significance and interest.

The article is arranged in the following order: Section 2 contains a description of the problem and formulation of governing equations, Section 3 presents the generalization of the developed model to fractional model along with analytic solutions, Section 4 discusses graphical and tabular results, and concluding remarks are provided in Section 5.

2. Description and modeling of the problem

In this investigation, we have considered the boundary driven MHD flow of a chemically reacted and electrically insulated Walters' B fluid close to an unbounded surface. The upright wall situated along the vertical direction (marked as x'-axis) is encountering the radiative effects in the horizontal direction (labeled as y'-axis). The geometry of the considered problem is configured in Figure 1 in terms of the Cartesian system. Initially, for $t' = 0$, the wall and fluid are static with concentration Φ'_∞ and temperature Θ'_∞. Later for $0 < t' \leq t'_0$, the boundary wall develops the flow of fluid due to its time-controlled motion with velocity $\Im'_0(t'/t'_0)$. For the same time interval, concentration and energy levels of the wall are maintained as $\Phi'_\infty + \Delta\Phi'(t'/t'_0)$ and $\Theta'_\infty + \Delta\Theta'(t'/t'_0)$ respectively. After this time duration, the wall expresses a uniform movement with velocity $\Im'_0$, and concentration and temperature are respectively changed to constant values as Φ'_w and Θ'_w, for $t' > t'_0$.

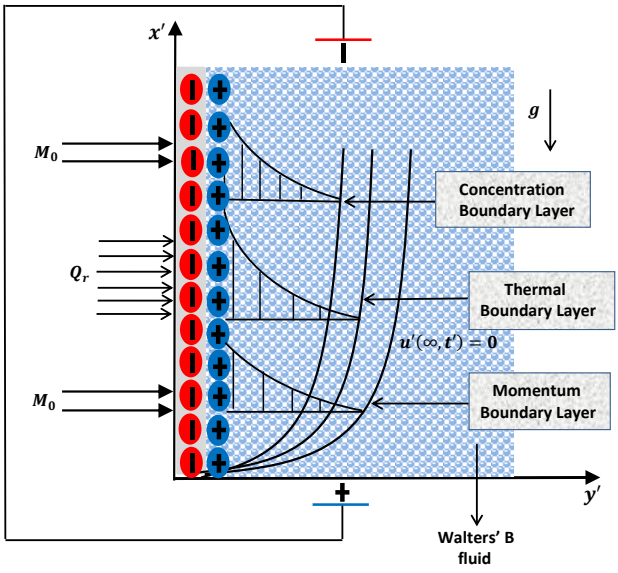

Figure 1. Geometrical display of the under observation problem.

Using expressions from the appendix, the final form of momentum equation is given along with energy and concentration equations

$$\rho\frac{\partial u'}{\partial t'} = \mu\frac{\partial^2 u'}{\partial y'^2} - \kappa_0\frac{\partial^3 u'}{\partial t'\partial y'^2} + \rho g\beta_1(\Theta' - \Theta'_\infty) + \rho g\beta_2(\Phi' - \Phi'_\infty)$$
$$+E_x\rho_e - \sigma M_0^2 u' - \frac{\mu\varphi}{\kappa_1}u' - \frac{\varphi\kappa_0}{\kappa_1}\frac{\partial u'}{\partial t'}, \tag{2.1}$$

$$\frac{\partial\Theta'}{\partial t'} = \frac{\kappa_2}{C_p\rho}\frac{\partial^2\Theta'}{\partial y'^2} + \frac{Q_1}{C_p\rho}(\Theta' - \Theta'_\infty) - \frac{1}{C_p\rho}\frac{\partial Q_r}{\partial y'}, \tag{2.2}$$

$$\frac{\partial\Phi'}{\partial t'} = D\frac{\partial^2\Phi'}{\partial y'^2} - R'(\Phi' - \Phi'_\infty). \tag{2.3}$$

In the modeled equations, C_p is the heat capacitance, κ_2 denotes the thermal conductance, Θ' represents the fluid's temperature, φ is the porosity parameter, Q_1 is the thermal injection/absorption coefficient, Q_r stands for thermal radiative flux, D accounts for the mass diffusion, R' specifies the rate of chemical reaction, u' is the fluid's velocity, $\mathfrak{I}'_0$ indicates the characteristic velocity, σ is the electrical conductance, κ_1 is the porosity of medium, κ_0 is the parameter associated with Walters' B fluid. Moreover, ρ and g are standard notations presenting density and gravitational pull respectively. The mathematical presentation of connected initial conditions and ramped surface conditions is

$$\text{For } y' \geq 0;\ u'(y',0) = 0,\ \Theta'(y',0) = \Theta'_\infty,\ \Phi'(y',0) = \Phi'_\infty, \tag{2.4}$$

$$\text{For } t' \leq t_0;\quad \begin{cases} u'(0,t') = \mathfrak{I}'_0\frac{t'}{t'_0} \\ \Theta'(0,t') = \Theta'_\infty + \Delta\Theta'\frac{t'}{t'_0} \\ \Phi'(0,t') = \Phi'_\infty + \Delta\Phi'\frac{t'}{t'_0} \end{cases}, \tag{2.5}$$

$$\text{For } t' > t'_0;\quad \begin{cases} u'(0,t') = \mathfrak{I}'_0 \\ \Theta'(0,t') = \Theta'_w \\ \Phi'(0,t') = \Phi'_w \end{cases}, \tag{2.6}$$

$$\text{For } y' \to \infty;\ u'(y',t') \to 0,\ \Theta'(y',t') \to \Theta'_\infty,\ \Phi'(y',t') \to \Phi'_\infty. \tag{2.7}$$

Under Rosseland approximation [51], the total thermal radiation flux is approximated as

$$Q_r = -\frac{4\varepsilon_r}{3\kappa_r}\frac{\partial\Theta'^4}{\partial y'}. \tag{2.8}$$

The above expression is nonlinear in terms of temperature function (Θ'^4). This term is expanded around Θ'_∞ through the Taylor series to obtain a linearized version of temperature function. Assuming sufficiently small temperature differences yields

$$\Theta'^4 \approx \Theta'_\infty(4\Theta'\Theta'^2_\infty - 3\Theta'^3_\infty). \tag{2.9}$$

Providing Eqs (2.8) and (2.9) in Eq (2.2) yields

$$\frac{\partial\Theta'}{\partial t'} = \frac{\kappa_2}{C_p\rho}\left(\frac{\partial^2\Theta'}{\partial y'^2} + \frac{16\varepsilon_r\Theta_\infty'^3}{3\kappa_2\kappa_r}\frac{\partial^2\Theta'}{\partial y'^2}\right) + \frac{Q_1}{C_p\rho}(\Theta' - \Theta_\infty'). \tag{2.10}$$

To make the problem independent of geometry and to reduce the number of parameters, the following unit-free quantities are employed

$$\Phi = \frac{\Phi' - \Phi_\infty'}{\Delta\Phi'}, \quad \Theta = \frac{\Theta' - \Theta_\infty'}{\Delta\Theta'}, \quad \Psi = \frac{u'}{\Im_0'}, \quad t = \frac{\Im_0'^2 t'}{\nu}, \quad \zeta = \frac{\Im_0' y'}{\nu}, \tag{2.11}$$

into Eqs (2.1), (2.3)–(2.7), and (2.10). This substitution gives the following modified model

$$a_1\frac{\partial\Psi}{\partial t} = \frac{\partial^2\Psi}{\partial\zeta^2} - a_2\Psi + Gr_1\Theta + Gr_2\Phi - E_s e^{-\kappa_3\zeta} - W_f\left(\frac{\partial^3\Psi}{\partial t\partial\zeta^2}\right), \tag{2.12}$$

$$Pr\frac{\partial\Theta}{\partial t} = \frac{\partial^2\Theta}{\partial\zeta^2} + R\frac{\partial^2\Theta}{\partial\zeta^2} + (QPr)\Theta, \tag{2.13}$$

$$Sc\frac{\partial\Phi}{\partial t} = \frac{\partial^2\Phi}{\partial\zeta^2} - (C_R Sc)\Phi, \tag{2.14}$$

$$\Psi(\zeta,0) = 0, \quad \Theta(\zeta,0) = 0, \quad \Phi(\zeta,0) = 0 \quad \text{for} \quad \zeta \geq 0, \tag{2.15}$$

$$\Psi(0,t) = \Theta(0,t) = \Phi(0,t) = \begin{cases} t & t \leq 1 \\ 1 & t > 1 \end{cases}, \tag{2.16}$$

$$\Psi(\zeta,t) \to 0, \quad \Theta(\zeta,t) \to 0, \quad \Phi(\zeta,t) \to 0 \quad \text{for} \quad \zeta \to \infty, \tag{2.17}$$

where $a_1 = 1 + \frac{W_f}{K}$, $a_2 = M + \frac{1}{K}$, and $\kappa_3 = \frac{\kappa_e\mu}{\rho\Im_0'}$ are constants, $K = \frac{\kappa_1\Im_0'^2}{\nu^2\varphi}$ specifies the permeability parameter, $C_R = \frac{\nu R'}{\Im_0'^2}$ is the parameter of chemical reaction, $Q = \frac{\mu Q_1}{\rho^2\Im_0'^2 C_p}$ accounts for the heat injected or absorbed, $M = \frac{\sigma M_0^2\nu}{\rho\Im_0'^2}$ denotes the magnetic strength, $Gr_1 = \frac{g\Delta\Theta'\nu\beta_1}{\Im_0'^3}$ is the thermal Grashof number, $Sc = \frac{\nu}{D}$ is the Schmidt number, $Pr = \frac{\mu C_p}{\kappa_2}$ represents the Prandtl number, $Gr_2 = \frac{g\Delta\Phi'\nu\beta_1}{\Im_0'^3}$ is the mass Grashof number, $R = \frac{16\varepsilon_r\Theta_\infty'^3}{3\kappa_2\kappa_r}$ characterizes the radiation effects, $E_s = \frac{\nu E_x\varepsilon\kappa_e^2\psi_w}{\rho\Im_0'^3}$ deals with electro-osmosis effects, and $W_f = \frac{\Im_0'^2 k_0}{\nu^2\rho}$ is the term associated with Walters' B fluid.

3. Generalization of model and computation of exact solutions

3.1. Fractional-order equations

The obtained unit-free model is transmuted to fractional form by substituting the integer-order time derivative $\left(\frac{\partial}{\partial t}\right)$ with Atangana-Baleanu fractional derivative $\left({}^{AB}\mathscr{D}_t^{\psi}\right)$. This substitution gives the following version of Eqs (2.12)–(2.14)

$$a_1\left\{{}^{AB}\mathscr{D}_t^{\psi}(\Psi)\right\} = \frac{\partial^2\Psi}{\partial\zeta^2} - a_2\Psi + Gr_1\Theta + Gr_2\Phi - E_s e^{-\kappa_3\zeta} - W_f\left\{{}^{AB}\mathscr{D}_t^{\psi}\left(\frac{\partial^2\Psi}{\partial\zeta^2}\right)\right\}, \tag{3.1}$$

$$Pr\left\{{}^{AB}\mathscr{D}_t^{\psi}(\Theta)\right\} = \frac{\partial^2\Theta}{\partial\zeta^2} + R\frac{\partial^2\Theta}{\partial\zeta^2} + (QPr)\Theta, \tag{3.2}$$

$$Sc\left\{{}^{AB}\mathscr{D}_t^{\psi}(\Phi)\right\} = \frac{\partial^2\Phi}{\partial\zeta^2} - (C_R Sc)\Phi. \tag{3.3}$$

For any fractional order ψ and an arbitrary function $F(t)$, expressions for Atangana-Baleanu derivative and its Laplace transform (LT) are presented as [45]

$${}^{AB}\mathscr{D}_t^{\psi}\left\{F(t)\right\} = \frac{1}{1-\psi}\int_0^t F'(z)E_{\psi}\left[-\psi\frac{(t-z)^{\psi}}{1-\psi}\right]dz, \text{ for } 0<\psi<1,$$

$$\mathscr{L}\left[{}^{AB}\mathscr{D}_t^{\psi}\left\{F(t)\right\}\right] = \frac{p^{\psi}\mathscr{L}\{F(t)\} - p^{\psi-1}F(0)}{p^{\psi}(1-\psi)+\psi},$$

where generalized Mittag-Leffler function is presented as

$$E_{\psi}(-t^{\psi}) = \sum_{q=0}^{\infty}\frac{(-t)^{\psi q}}{\Gamma(1+\psi q)}.$$

3.2. Solutions of fractional equations

Applying the LT on Eq (3.2) and solving as

$$\mathscr{L}\left\{{}^{AB}\mathscr{D}_t^{\psi}(\Theta)\right\} = \mathscr{L}\left\{a_3\frac{\partial^2\Theta}{\partial\zeta^2} + Q\Theta\right\},$$

$$\left(\frac{p^{\psi}}{p^{\psi}+\frac{\psi}{1-\psi}}\times\frac{1}{1-\psi}\right)\bar{\Theta} - Q\bar{\Theta} = a_3\frac{d^2\bar{\Theta}}{d\zeta^2},$$

$$\frac{d^2\bar{\Theta}}{d\zeta^2} = \frac{1}{a_3}\left(\frac{p^{\psi}b_0}{p^{\psi}+b_1} - Q\right)\bar{\Theta},$$

$$\frac{d^2\bar{\Theta}}{d\zeta^2} - \chi_1\left(\frac{p^{\psi}-b_2}{p^{\psi}+b_1}\right)\bar{\Theta} = 0. \tag{3.4}$$

The general solution of Eq (3.4) is determined by employing the method of undetermined coefficients as

$$\bar{\Theta}(\zeta,p) = C_1\exp\left(\zeta\sqrt{\chi_1\frac{p^{\psi}-b_2}{p^{\psi}+b_1}}\right) + C_2\exp\left(-\zeta\sqrt{\chi_1\frac{p^{\psi}-b_2}{p^{\psi}+b_1}}\right). \tag{3.5}$$

The Laplace transformed boundary conditions are used to find the following values of involved constants C_1 and C_2

$$C_1 = 0 \quad \text{and} \quad C_2 = \frac{1 - e^{-p}}{p^2}.$$

Providing the values of C_1 and C_2 in Eq (3.5), we acquire

$$\bar{\Theta}(\zeta, p) = \frac{1 - e^{-p}}{p^2} \exp\left(- \sqrt{\chi_1 \frac{p^{\psi} - b_2}{p^{\psi} + b_1}} \zeta \right). \tag{3.6}$$

Similar steps are adapted to construct a solution of the concentration field (Eq (3.3)) however, avoiding the writing repetition, the final form of general concentration solution is presented as

$$\bar{\Phi}(\zeta, p) = \frac{1 - e^{-p}}{p^2} \exp\left(- \sqrt{\chi_2 \frac{p^{\psi} + a_5}{p^{\psi} + b_1}} \zeta \right), \tag{3.7}$$

where

$$a_3 = \frac{1 + R}{Pr}, \quad a_4 = C_R S c, \quad a_5 = \frac{b_1 a_4}{\chi_2}, \quad b_0 = \frac{1}{1 - \psi},$$
$$b_1 = \psi b_0, \quad b_2 = \frac{b_1 Q}{b_0 - Q}, \quad \chi_1 = \frac{b_0 - Q}{a_3}, \quad \chi_2 = b_0 S c + a_4.$$

Now incorporating the LT into Eq (3.1) gives us the following velocity equation

$$\left(\frac{b_4 p^{\psi} + b_1}{p^{\psi} + b_1} \right) \frac{d^2 \bar{\Psi}}{d\zeta^2} - \left(\frac{b_3 p^{\psi} + a_2 b_1}{p^{\psi} + b_1} \right) \bar{\Psi} = \frac{E_s}{p} e^{-\kappa_3 \zeta} - Gr_1 \bar{\Theta} - Gr_2 \bar{\Phi}. \tag{3.8}$$

Plugging Eqs (3.6) and (3.7) in Eq (3.8) and solving the consequent equation, the following general velocity expression is evaluated

$$\begin{aligned} \bar{\Psi}(\zeta, p) = {} & D_1 \exp\left(\sqrt{\chi_3 \frac{p^{\psi} + b_5}{p^{\psi} + b_6}} \zeta \right) + D_2 \exp\left(- \sqrt{\chi_3 \frac{p^{\psi} + b_5}{p^{\psi} + b_6}} \zeta \right) \\ & - \frac{Gr_3 (1 - e^{-p})(p^{\psi} + b_1)^2}{(\Gamma_1 p^{2\psi} + \Gamma_2 p^{\psi} - \Gamma_3)\, p^2} \exp\left(- \sqrt{\chi_1 \frac{p^{\psi} - b_2}{p^{\psi} + b_1}} \zeta \right) \\ & - \frac{Gr_4 (1 - e^{-p})(p^{\psi} + b_1)^2}{(\Gamma_4 p^{2\psi} + \Gamma_5 p^{\psi} - \Gamma_6)\, p^2} \exp\left(- \sqrt{\chi_2 \frac{p^{\psi} + a_5}{p^{\psi} + b_1}} \zeta \right) \\ & + \frac{E_0 (p^{\psi} + b_1) e^{-\kappa_3 \zeta}}{\{p^{\psi} + b_6 - b_7 (p^{\psi} - a_6)\}\, p}. \end{aligned} \tag{3.9}$$

Determining the constants D_1 and D_2 through related boundary conditions and substituting them in Eq (3.9) yields

$$\begin{aligned}\bar{\Psi}(\zeta,p) = {} & \frac{1-e^{-p}}{p^2}\exp\left(-\sqrt{\chi_3\frac{p^\psi+b_5}{p^\psi+b_6}}\zeta\right)\\ & + \frac{Gr_5(1-e^{-p})(p^\psi+b_1)^2}{(p^\psi+m_1)(p^\psi+m_2)p^2}\exp\left(-\sqrt{\chi_3\frac{p^\psi+b_5}{p^\psi+b_6}}\zeta\right)\\ & + \frac{Gr_6(1-e^{-p})(p^\psi+b_1)^2}{(p^\psi+m_3)(p^\psi+m_4)p^2}\exp\left(-\sqrt{\chi_3\frac{p^\psi+b_5}{p^\psi+b_6}}\zeta\right)\\ & - \frac{E_0(p^\psi+b_1)}{\{p^\psi+b_6-b_7(p^\psi-a_6)\}\,p}\exp\left(-\sqrt{\chi_3\frac{p^\psi+b_5}{p^\psi+b_6}}\zeta\right)\\ & - \frac{Gr_5(1-e^{-p})(p^\psi+b_1)^2}{(p^\psi+m_1)(p^\psi+m_2)p^2}\exp\left(-\sqrt{\chi_1\frac{p^\psi-b_2}{p^\psi+b_1}}\zeta\right)\\ & - \frac{Gr_6(1-e^{-p})(p^\psi+b_1)^2}{(p^\psi+m_3)(p^\psi+m_4)p^2}\exp\left(-\sqrt{\chi_2\frac{p^\psi+a_5}{p^\psi+b_1}}\zeta\right)\\ & + \frac{E_0(p^\psi+b_1)}{\{p^\psi+b_6-b_7(p^\psi-a_6)\}\,p}\exp\left(-\kappa_3\zeta\right), \end{aligned} \tag{3.10}$$

where

$$\begin{gathered} b_3 = b_0a_1+a_2,\ b_4 = 1-b_0W_f,\ b_5 = \frac{b_1a_2}{b_3},\ b_6 = \frac{b_1}{b_4},\ b_7 = \frac{b_3}{b_4k_3^2},\ \chi_3 = \frac{b_3}{b_4},\\ \Gamma_1 = \chi_1-\chi_3,\ \Gamma_2 = b_6\chi_1-b_2\chi_1-b_1\chi_3-b_5\chi_3,\ \Gamma_3 = b_2b_6\chi_1+b_1b_5\chi_3,\\ \Gamma_4 = \chi_2-\chi_3,\ \Gamma_5 = b_6\chi_2+a_5\chi_2-b_1\chi_3-b_5\chi_3,\ \Gamma_6 = b_1b_5\chi_3-b_6a_5\chi_2,\\ E_0 = \frac{E_s}{b_4\kappa_3^2},\ Gr_3 = \frac{Gr_1}{b_4},\ Gr_4 = \frac{Gr_2}{b_4},\ Gr_5 = \frac{Gr_3}{\Gamma_1},\\ Gr_6 = \frac{Gr_4}{\Gamma_4},\ B_1 = \frac{\Gamma_2}{\Gamma_1},\ B_2 = -\frac{\Gamma_3}{\Gamma_1},\ B_3 = \frac{\Gamma_5}{\Gamma_4},\\ B_4 = -\frac{\Gamma_6}{\Gamma_4},\ m_1 = \frac{B_1+\sqrt{B_1^2-4B_2}}{2},\ m_2 = \frac{B_1-\sqrt{B_1^2-4B_2}}{2},\\ m_3 = \frac{B_3+\sqrt{B_3^2-4B_4}}{2},\ m_4 = \frac{B_3-\sqrt{B_3^2-4B_4}}{2},\ a_6-\frac{a_2b_1}{b_3}. \end{gathered}$$

Equation (3.10) can be simplified as

$$\bar{\Psi}(\zeta,p) = \frac{\gamma_1}{p^{2-\psi}}\frac{1-e^{-p}}{p^\psi}\exp\left(-\sqrt{\chi_3}\sqrt{\frac{p^\psi+b_5}{p^\psi+b_6}}\zeta\right)+\frac{\gamma_2}{p^{2-\psi}}\frac{1-e^{-p}}{p^\psi+m_1}\exp\left(-\sqrt{\chi_3}\sqrt{\frac{p^\psi+b_5}{p^\psi+b_6}}\zeta\right)$$

$$
\begin{aligned}
&+\frac{\gamma_3}{p^{2-\psi}}\frac{1-e^{-p}}{p^{\psi}+m_2}\exp\left(-\sqrt{\chi_3}\sqrt{\frac{p^{\psi}+b_5}{p^{\psi}+b_6}}\zeta\right)+\frac{\gamma_4}{p^{2-\psi}}\frac{1-e^{-p}}{p^{\psi}}\exp\left(-\sqrt{\chi_3}\sqrt{\frac{p^{\psi}+b_5}{p^{\psi}+b_6}}\zeta\right)\\
&+\frac{\gamma_5}{p^{2-\psi}}\frac{1-e^{-p}}{p^{\psi}+m_3}\exp\left(-\sqrt{\chi_3}\sqrt{\frac{p^{\psi}+b_5}{p^{\psi}+b_6}}\zeta\right)+\frac{\gamma_6}{p^{2-\psi}}\frac{1-e^{-p}}{p^{\psi}+m_4}\exp\left(-\sqrt{\chi_3}\sqrt{\frac{p^{\psi}+b_5}{p^{\psi}+b_6}}\zeta\right)\\
&-\frac{\gamma_7}{p^{1-\psi}}\frac{1}{p^{\psi}}\exp\left(-\sqrt{\chi_3}\sqrt{\frac{p^{\psi}+b_5}{p^{\psi}+b_6}}\zeta\right)-\frac{\gamma_8}{p^{1-\psi}}\frac{1}{p^{\psi}+b_8}\exp\left(-\sqrt{\chi_3}\sqrt{\frac{p^{\psi}+b_5}{p^{\psi}+b_6}}\zeta\right)\\
&-\frac{\gamma_1}{p^{2-\psi}}\frac{1-e^{-p}}{p^{\psi}}\exp\left(-\sqrt{\chi_1}\sqrt{\frac{p^{\psi}-b_2}{p^{\psi}+b_1}}\zeta\right)-\frac{\gamma_2}{p^{2-\psi}}\frac{1-e^{-p}}{p^{\psi}+m_1}\exp\left(-\sqrt{\chi_1}\sqrt{\frac{p^{\psi}-b_2}{p^{\psi}+b_1}}\zeta\right)\\
&-\frac{\gamma_3}{p^{2-\psi}}\frac{1-e^{-p}}{p^{\psi}+m_2}\exp\left(-\sqrt{\chi_1}\sqrt{\frac{p^{\psi}-b_2}{p^{\psi}+b_1}}\zeta\right)-\frac{\gamma_4}{p^{2-\psi}}\frac{1-e^{-p}}{p^{\psi}}\exp\left(-\sqrt{\chi_2}\sqrt{\frac{p^{\psi}+a_5}{p^{\psi}+b_1}}\zeta\right)\\
&-\frac{\gamma_5}{p^{2-\psi}}\frac{1-e^{-p}}{p^{\psi}+m_3}\exp\left(-\sqrt{\chi_2}\sqrt{\frac{p^{\psi}+a_5}{p^{\psi}+b_1}}\zeta\right)-\frac{\gamma_6}{p^{2-\psi}}\frac{1-e^{-p}}{p^{\psi}+m_4}\exp\left(-\sqrt{\chi_2}\sqrt{\frac{p^{\psi}+a_5}{p^{\psi}+b_1}}\zeta\right)\\
&+\frac{\gamma_7}{p^{1-\psi}}\frac{1}{p^{\psi}}\exp\left(-\kappa_3\zeta\right)+\frac{\gamma_8}{p^{1-\psi}}\frac{1}{p^{\psi}+b_8}\exp\left(-\kappa_3\zeta\right),
\end{aligned}
\tag{3.11}
$$

where

$$
b_8=\frac{b_6+a_6b_7}{1-b_7},\ \gamma_1=1+\frac{Gr_5b_1^2}{\Gamma_1\Gamma_2},\ \gamma_2=\frac{Gr_5(b_1-\Gamma_1)^2}{\Gamma_1(\Gamma_1-\Gamma_2)},\ \gamma_3=\frac{Gr_5(b_1-\Gamma_2)^2}{\Gamma_2(\Gamma_2-\Gamma_1)},
$$
$$
\gamma_4=\frac{Gr_6b_1^2}{\Gamma_3\Gamma_4},\ \gamma_5=\frac{Gr_6(b_1-\Gamma_3)^2}{\Gamma_3(\Gamma_3-\Gamma_4)},\ \gamma_6=\frac{Gr_6(b_1-\Gamma_4)^2}{\Gamma_4(\Gamma_4-\Gamma_3)},
$$
$$
\gamma_7=\frac{E_0b_1}{b_6+a_6b_7},\ \gamma_8=E_0\left(1-b_1\frac{1-b_7}{b_6+a_6b_7}\right).
$$

The more adequate form of Eqs (3.6), (3.7), and (3.11) for Laplace inversion is stated as

$$
\bar{\Theta}(\zeta,p)=\frac{1}{p^{2-\psi}}\bar{\mathfrak{R}}(-\sqrt{\chi_1}\zeta,p,0,1,-b_2,b_1),
\tag{3.12}
$$

$$
\bar{\Phi}(\zeta,p)=\frac{1}{p^{2-\psi}}\bar{\mathfrak{R}}(-\sqrt{\chi_2}\zeta,p,0,1,a_5,b_1),
\tag{3.13}
$$

$$
\begin{aligned}
\bar{\Psi}(\zeta,p)=&\frac{\gamma_1(1-e^{-p})}{p^{2-\psi}}\bar{\mathfrak{R}}(-\sqrt{\chi_3}\zeta,p,0,1,b_5,b_6)+\frac{\gamma_2(1-e^{-p})}{p^{2-\psi}}\bar{\mathfrak{R}}(-\sqrt{\chi_3}\zeta,p,m_1,1,b_5,b_6)\\
&+\frac{\gamma_3(1-e^{-p})}{p^{2-\psi}}\bar{\mathfrak{R}}(-\sqrt{\chi_3}\zeta,p,m_2,1,b_5,b_6)+\frac{\gamma_4(1-e^{-p})}{p^{2-\psi}}\bar{\mathfrak{R}}(-\sqrt{\chi_3}\zeta,p,0,1,b_5,b_6)\\
&+\frac{\gamma_5(1-e^{-p})}{p^{2-\psi}}\bar{\mathfrak{R}}(-\sqrt{\chi_3}\zeta,p,m_3,1,b_5,b_6)+\frac{\gamma_6(1-e^{-p})}{p^{2-\psi}}\bar{\mathfrak{R}}(-\sqrt{\chi_3}\zeta,p,m_4,1,b_5,b_6)\\
&-\frac{\gamma_7}{p^{1-\psi}}\bar{\mathfrak{R}}(-\sqrt{\chi_3}\zeta,p,0,1,b_5,b_6)-\frac{\gamma_8}{p^{1-\psi}}\bar{\mathfrak{R}}(-\sqrt{\chi_3}\zeta,p,b_8,1,b_5,b_6)
\end{aligned}
$$

$$
\begin{aligned}
&- \frac{\gamma_1(1-e^{-p})}{p^{2-\psi}}\bar{\mathfrak{R}}(-\sqrt{\chi_1}\zeta, p, 0, 1, -b_2, b_1) - \frac{\gamma_2(1-e^{-p})}{p^{2-\psi}}\bar{\mathfrak{R}}(-\sqrt{\chi_1}\zeta, p, m_1, 1, -b_2, b_1)\\
&- \frac{\gamma_3(1-e^{-p})}{p^{2-\psi}}\bar{\mathfrak{R}}(-\sqrt{\chi_1}\zeta, p, m_2, 1, -b_2, b_1) - \frac{\gamma_4(1-e^{-p})}{p^{2-\psi}}\bar{\mathfrak{R}}(-\sqrt{\chi_2}\zeta, p, 0, 1, a_5, b_1)\\
&- \frac{\gamma_5(1-e^{-p})}{p^{2-\psi}}\bar{\mathfrak{R}}(-\sqrt{\chi_2}\zeta, p, m_3, 1, a_5, b_1) - \frac{\gamma_6(1-e^{-p})}{p^{2-\psi}}\bar{\mathfrak{R}}(-\sqrt{\chi_2}\zeta, p, m_4, 1, a_5, b_1)\\
&+ \frac{\gamma_7}{p^{1-\psi}}\frac{1}{p^{\psi}}\exp(-\kappa_3\zeta) + \frac{\gamma_8}{p^{1-\psi}}\frac{1}{p^{\psi}+b_8}\exp(-\kappa_3\zeta). \qquad (3.14)
\end{aligned}
$$

Equations (3.12), (3.13), and (3.14) are transmuted back in primary coordinates (ζ, t) by employing the Laplace inversion technique. The real-time solutions are furnished as

$$
\begin{aligned}
\Theta(\zeta,t) &= F_1(t) * \mathfrak{R}(-\sqrt{\chi_1}\zeta, t, 0, 1, -b_2, b_1) - H(t_1)\Big\{F_1(t_1) * \mathfrak{R}(-\sqrt{\chi_1}\zeta, t_1, 0, 1, -b_2, b_1)\Big\}, \qquad (3.15)\\
\Phi(\zeta,t) &= F_1(t) * \mathfrak{R}(-\sqrt{\chi_2}\zeta, t, 0, 1, a_5, b_1) - H(t_1)\Big\{F_1(t_1) * \mathfrak{R}(-\sqrt{\chi_1}\zeta, t_1, 0, 1, a_5, b_1)\Big\}, \qquad (3.16)\\
\Psi(\zeta,t) &= F_1(t) * \gamma_9\mathfrak{R}(-\sqrt{\chi_3}\zeta, t, 0, 1, b_5, b_6) - H(t_1)\Big\{F_1(t_1) * \gamma_9\mathfrak{R}(-\sqrt{\chi_3}\zeta, t_1, 0, 1, b_5, b_6)\Big\}\\
&+ F_1(t) * \gamma_2\mathfrak{R}(-\sqrt{\chi_3}\zeta, t, m_1, 1, b_5, b_6) - H(t_1)\Big\{F_1(t_1) * \gamma_2\mathfrak{R}(-\sqrt{\chi_3}\zeta, t_1, m_1, 1, b_5, b_6)\Big\}\\
&+ F_1(t) * \gamma_3\mathfrak{R}(-\sqrt{\chi_3}\zeta, t, m_2, 1, b_5, b_6) - H(t_1)\Big\{F_1(t_1) * \gamma_3\mathfrak{R}(-\sqrt{\chi_3}\zeta, t_1, m_2, 1, b_5, b_6)\Big\}\\
&+ F_1(t) * \gamma_5\mathfrak{R}(-\sqrt{\chi_3}\zeta, t, m_3, 1, b_5, b_6) - H(t_1)\Big\{F_1(t_1) * \gamma_5\mathfrak{R}(-\sqrt{\chi_3}\zeta, t_1, m_3, 1, b_5, b_6)\Big\}\\
&+ F_1(t) * \gamma_6\mathfrak{R}(-\sqrt{\chi_3}\zeta, t, m_4, 1, b_5, b_6) - H(t_1)\Big\{F_1(t_1) * \gamma_6\mathfrak{R}(-\sqrt{\chi_3}\zeta, t_1, m_4, 1, b_5, b_6)\Big\}\\
&- F_2(t) * \gamma_7\mathfrak{R}(-\sqrt{\chi_3}\zeta, t, 0, 1, b_5, b_6) - F_2(t) * \gamma_8\mathfrak{R}(-\sqrt{\chi_3}\zeta, t, b_8, 1, b_5, b_6)\\
&- F_1(t) * \gamma_1\mathfrak{R}(-\sqrt{\chi_1}\zeta, t, 0, 1, -b_2, b_1) + H(t_1)\Big\{F_1(t_1) * \gamma_1\mathfrak{R}(-\sqrt{\chi_1}\zeta, t_1, 0, 1, -b_2, b_1)\Big\}\\
&- F_1(t) * \gamma_2\mathfrak{R}(-\sqrt{\chi_1}\zeta, t, m_1, 1, -b_2, b_1) + H(t_1)\Big\{F_1(t_1) * \gamma_2\mathfrak{R}(-\sqrt{\chi_1}\zeta, t_1, m_1, 1, -b_2, b_1)\Big\}\\
&- F_1(t) * \gamma_3\mathfrak{R}(-\sqrt{\chi_1}\zeta, t, m_2, 1, -b_2, b_1) + H(t_1)\Big\{F_1(t_1) * \gamma_3\mathfrak{R}(-\sqrt{\chi_1}\zeta, t_1, m_2, 1, -b_2, b_1)\Big\}\\
&- F_1(t) * \gamma_4\mathfrak{R}(-\sqrt{\chi_2}\zeta, t, 0, 1, a_5, b_1) + H(t_1)\Big\{F_1(t_1) * \gamma_4\mathfrak{R}(-\sqrt{\chi_2}\zeta, t_1, 0, 1, a_5, b_1)\Big\}\\
&- F_1(t) * \gamma_5\mathfrak{R}(-\sqrt{\chi_2}\zeta, t, m_3, 1, a_5, b_1) + H(t_1)\Big\{F_1(t_1) * \gamma_5\mathfrak{R}(-\sqrt{\chi_2}\zeta, t_1, m_3, 1, a_5, b_1)\Big\}\\
&- F_1(t) * \gamma_6\mathfrak{R}(-\sqrt{\chi_2}\zeta, t, m_4, 1, a_5, b_1) + H(t_1)\Big\{F_1(t_1) * \gamma_6\mathfrak{R}(-\sqrt{\chi_2}\zeta, t_1, m_4, 1, a_5, b_1)\Big\}\\
&+ F_2(t) * \gamma_7\exp(-\kappa_3\zeta)R_{(\psi,0)}(0,t) + F_2(t) * \gamma_8\exp(-\kappa_3\zeta)R_{(\psi,0)}(-b_8,t), \qquad (3.17)
\end{aligned}
$$

where * denotes the convolution product and

$$
\gamma_9 = \gamma_1 + \gamma_4, \quad \mathscr{L}^{-1}\left(\frac{1}{p^{\psi}}\right) = R_{(\psi,0)}(0,t), \quad \mathscr{L}^{-1}\left(\frac{1}{p^{\psi}+b_8}\right) = R_{(\psi,0)}(-b_8,t),
$$

$$
\mathscr{L}^{-1}\left(\frac{1}{p^{2-\psi}}\right) = F_1(t) = \frac{t^{1-\psi}}{\Gamma(2-\psi)}, \quad \mathscr{L}^{-1}\left(\frac{1}{p^{1-\psi}}\right) = F_2(t) = \frac{1}{t^{\psi}\Gamma(1-\psi)},
$$

$$
\mathfrak{R}(\zeta, t, \omega_1, \omega_2, \omega_3, \omega_4) = \frac{1}{\pi}\int_0^{\infty}\int_0^{\infty}\Omega_1(\zeta, t, \omega_1, \omega_2, \omega_3, \omega_4)
$$

$$\times \exp(-\nu n^{\psi}\cos\pi\psi - nt)\sin(\nu n^{\psi}\sin\pi\psi)dnd\nu,$$

$$\Omega_1(\zeta,t,\omega_1,\omega_2,\omega_3,\omega_4) = e^{-\omega_1 t-\sqrt{\omega_2}\zeta} - \sqrt{\frac{b_9}{\pi}}\frac{\zeta}{2}\int_0^{\infty}\int_0^{t}\frac{e^{-\omega_1 t}}{\sqrt{t}}I_1\left(2\sqrt{b_9}\nu t\right)$$

$$\times \exp\left(\omega_1 t - \omega_2\nu - \omega_4 t - \frac{\zeta^2}{4\nu}\right)dtd\nu, \quad b_9 = \omega_3 - \omega_2\omega_4.$$

3.3. Some significant quantities

Proceeding for the effective measurement of shear stress and rates of mass and heat transmission, the coefficient of skin friction (C_f), Sherwood number (Sh), and Nusselt number (Nu) are described as

$$C_f = \left(\mu - \kappa_0\frac{\partial}{\partial t'}\right)\frac{\partial u'}{\partial y'}\bigg|_{y'=0}, \quad Sh = \frac{h^*\nu}{D(\Delta\Phi')\Im_0'}, \quad Nu = \frac{q^*\nu}{\kappa_2(\Delta\Theta')\Im_0'}, \tag{3.18}$$

where mass flux h^* and heat flux q^* are expressed as

$$h^* = -D\frac{\partial\Phi'}{\partial y'}\bigg|_{y'=0}, \quad q^* = -\kappa_2\frac{\partial\Theta'}{\partial y'}\bigg|_{y'=0}. \tag{3.19}$$

Providing relevant values from Eq (2.11) and substituting Eq (3.19), Eq (3.18) becomes

$$C_f = \left(1 - W_f\frac{\partial}{\partial t}\right)\frac{\partial\Psi}{\partial\zeta}\bigg|_{\zeta=0}, \quad Sh = -\frac{\partial\Phi}{\partial\zeta}\bigg|_{\zeta=0}, \quad Nu = -\frac{\partial\Theta}{\partial\zeta}\bigg|_{\zeta=0}. \tag{3.20}$$

4. Results and discussion

In this investigation, the concept of time-fractional Atangana-Baleanu derivative is applied to achieve the purpose of improved thermal efficiency of the electro-osmotic flow of Walters' B fluid over a permeable upright wall that expresses a ramped motion. This study also encounters thermal radiation, MHD, and heat injection/absorption phenomena. Besides this, the mass diffusion mechanism is also explored under first-order chemical reaction. After reviewing the literature, it is important to mention that ramped velocity, concentration, and energy boundary conditions are first time simultaneously employed for a non-Newtonian fluid. Operating these non-uniform conditions at the same time produces multiple intricate functions in terms of Laplace frequency, which sometimes restricts the execution of analytic Laplace inversion. However, in this work, exact real domain versions of all the primary functions (velocity, concentration, and temperature) are procured in integral form employing the analytic Laplace reversal technique. In this section, results of numerical simulations are provided through graphical illustrations and tabular arrangements to deeply probe the computational and physical attributes of the under observation problem. Some physical arguments are discussed to justify the portrayed fluctuations in behaviors of velocity, concentration, and temperature distributions subject to changes in correlated parameters. Since the levied boundary conditions are

piece-wise functions of time, therefore, all the tables and plots are constructed for a wide range of time values. In the end, the prominent contribution of fractional and other associated parameters in determining the shear stress and mass and heat transfer rates is anatomized by precisely computing the velocity, concentration, and energy gradients at the bounding wall.

Figures 2–4 respectively display the velocity, concentration, and energy solution profiles for fractional and classical models. These profiles are graphed and discussed for three values of the time. The first value of time is selected as $t = 0.7$, which highlights the behavior of functions for the time-dependent part of the corresponding boundary condition i.e., $t < 1$. The other two values of time are $t = 2.0$ and $t = 5.0$. These values account for that time portion of the boundary conditions for which the functions are independent of time and have constant value 1 i.e., $t > 1$. It is evident from Figures 2–4 that fractional parameter ψ declines the profiles of all three functions for $t < 1$ whereas, for $t > 1$, this trend reverses completely and functions exhibit increasing profiles. Moreover, it is witnessed that for smaller values of time, the fundamental functions involved in this study are maximum for the fractional model whereas, for $t > 1$, the classical model provides the highest profiles of these functions. The primary reason behind the aforementioned observations is that ψ exerts a dual nature influence on boundary layer thicknesses. For ramped condition, it attenuates the momentum boundary layer but for uniform surface condition, it causes to expand the thickness of the momentum boundary layer. This interpretation is also true for the expansion and attenuation of thermal and concentration boundary layers. These explanations certify that the graphical illustrations are in accordance with physical behaviors. The changes produced in the flow pattern due to the presence of magnetic lines of action are portrayed in Figure 5. Unlike ψ, the parameter M has uniform effects for all three values of t. It is recognized that the imposition of a magnetic field causes to slow down the flow of Walters' B fluid. The physical argument for this retardation is the generation of a highly effective viscous force, which drags the fluid in an anti-flow direction. This force is commonly termed as Lorentz force. The Lorentz force enables the viscous forces to eliminate the impacts of flow supportive forces, which leads to contract the momentum boundary layer thickness. In consequence, the curve associated with the velocity function continuously declines for enhancing domain of M.

The response of the velocity function for alteration in Gr_1 and Gr_2 is reported in Figures 6 and 7, respectively. It is deduced that both parameters have an identical influence on the flow pattern. The Walters' B fluid gets accelerated due to a rise in the magnitudes of Gr_1 and Gr_2. In the physical sense, Gr_1 and Gr_2 share an inverse correspondence with viscous effects and direct relation with buoyancy forces. In an alternative way, the Grashof number is a means of quantifying the two opposite forces. The buoyancy forces are credited as flow accelerated forces, which depend upon the temperature and concentration gradients. The rising values of Gr_1 and Gr_2 signify these gradients, and consequently, the buoyancy forces vanquish the control of viscous effects on the velocity function. These phenomena expand the thickness of corresponding boundary layers, and accelerated flow patterns are witnessed. Figure 8 features the velocity function to inspect the influence of the material parameter of Walters' B fluid W_f on the flow profile. The parameter W_f characterizes the elastic and viscous features of the material, and it is one of the key factors for the intensified viscoelastic nature of the Walters' B fluid. Hence, the rising magnitude of W_f increases the viscoelasticity of the fluid, which diminishes the flow speed and brings down the corresponding curve. The respective figure describes another stimulating result that the flow of the Newtonian fluid ($W_f = 0$) is more expeditious as equated to the flow of Walters' B fluid ($W_f \neq 0$). The specific factor responsible for this outcome is the lower

viscosity of a Newtonian fluid. With the aid of Figure 9, ramifications of nesting the upright ramped wall in a porous medium are discussed for the flow phenomenon. This figure indicates the existence of direct proportionality between fluid velocity and permeability parameter K. It means that the speed of the flow enhances for growing inputs of K, and there is a continuous rise in the associated curve. An enlargement in diameter of the permeable holes of the medium provides the physical supportive ground for this rise in the velocity. Additionally, one of the reasons for speedy flow is that more amount of fluid can penetrate through the porous medium due to the increased size of the holes. The observed outcome is also justified by the fact that the fluid confronts weak resistance type forces because of the greater volume capacity of the medium. The modulating consequences of R_d on flow patterns are analyzed through Figure 10. The anticipation of heat radiative gradient by means of Rosseland approximation communicates that the extended domain of R_d restricts the considered fluid to discharge the energy. Subsequently, the fluid particles possess high energy due to a greater amount of heat transmitted at the solid-fluid interface. The augmented energy level excites the particles, due to which they start performing rapid collisions. As a consequence of such collisions, cohesive forces become ineffective because of the breakage of inter-particle bonds. The existence of this mechanism implies that the resistive potential of fluid particles is weak. Hence, the fluid performs a high-speed motion for amplified inputs of R_d.

Figures 11 and 12 are drawn to feature the influences of Sc and C_R on the flow profile. These parameters appear in the velocity term because of the partial coupling of the flow and concentration equations. These figures describe that both the considered parameters have similar impacts on fluid velocity. Particularly these parameters lead to slow down the flow speed. Since Sc and viscous forces are directly linked to each other, therefore the deceleration in the flow is pretty obvious for this parameter because it signifies the viscous strength of the fluid and dwindles the mass diffusion. Identically, raising the value of the parameter C_R associated with corrosive chemical reaction minimizes the species concentration, which results in weaker solutal buoyancy forces. In this way, the velocity of the fluid is suppressed and a decaying profile is observed from the relevant figure. Figure 13 is a graphical demonstration of the contribution of Pr in setting the fluid flow. The thicknesses of momentum and thermal boundary layer are significantly influenced by Pr and also it is considered one of the vital parameters to examine the heat transfer problems. Physically, it inculcates the relative effects of viscosity and fluid's heat conduction capacity. From Figure 13, a decelerating flow field is witnessed for a rising variation of Pr. This is because the conduction capacity of fluids with large Pr is dominated by those having small Pr values. Moreover, the larger Pr values have the tendency to augment the momentum diffusivity, which enhances the thickness of fluids and make them more viscous. Taking everything into account, it can be stated that viscous influence permits the fluids to exhibit a controlled flow with restraint velocity. Hence, we perceive a dropping velocity profile in response to Pr maximization. The changes produced in the flow field for modification of E_s are recorded in Figure 14. It is discovered that the application of electro-osmotic force on Walters' B fluid provokes decelerating effects on the flow. From a physical view, the electric double layer attains more charges in consequence of the enhanced strength of the imposed electric field. Because of this charge intensification, the fluid gathers dominant resistive forces that restrict the fluid velocity. This control of electro-osmosis on the liquid flow has gathered vital applications in sub-branches of medical sciences, biochemical, and engineering. For example, separated fluids through electro-osmosis are effective as drug carriers, electronic controlling of liquid motions, minimizing the deterioration and

dampness of very thick wall structures [52], and materials processing [53]. The consequences of including a heat injector in the considered model on the velocity function are evaluated in Figure 15. This evaluation is conducted by choosing diverse values for the injection parameter Q, while magnitudes of other parameters are considered fixed. It is found that the velocity function escalates for growing values of Q. Since the energy of fluid particles is augmented for the boosted rate of heat injection at the solid-fluid interface, therefore the temperature of the particles rises. Following this reason, the forces functioning against the separation of fluid particles from each other become inefficient. Accordingly, the fluid describes a swift flow velocity.

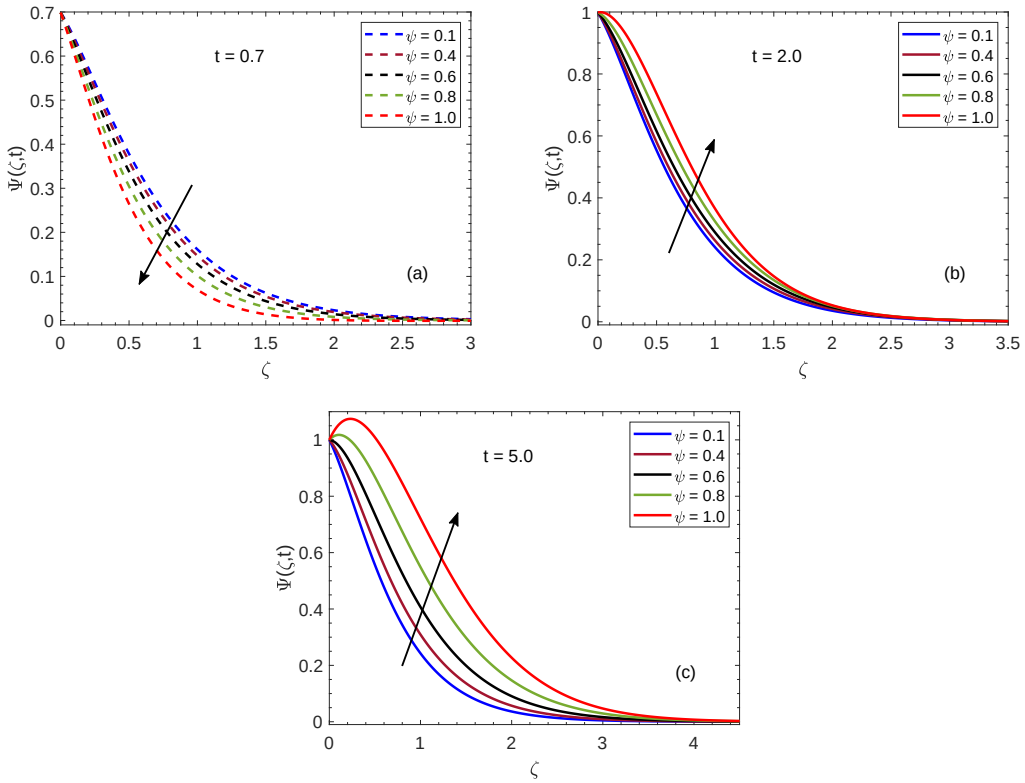

Figure 2. Velocity patterns for diverse magnitudes of ψ.

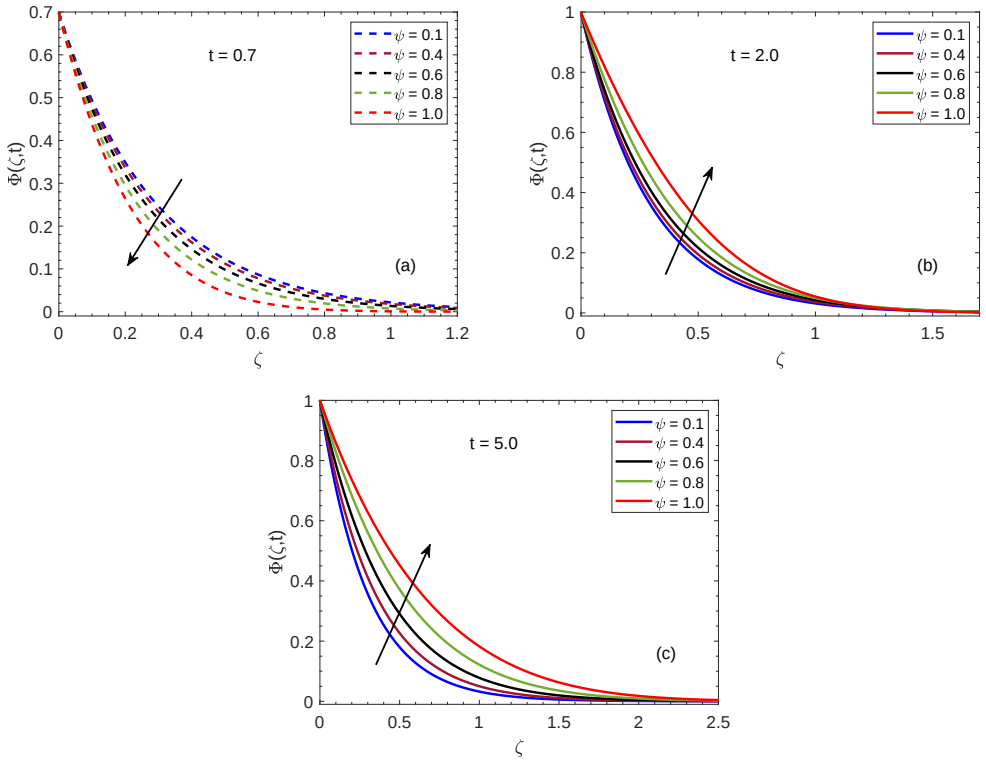

Figure 3. Concentration curves for diverse magnitudes of ψ.

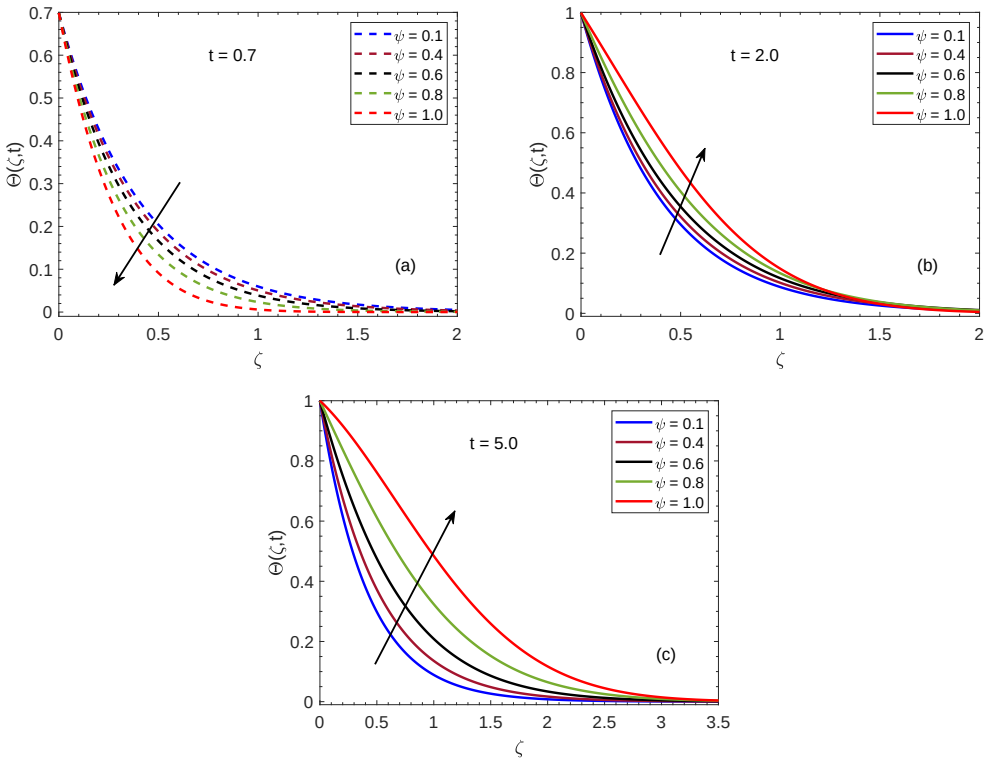

Figure 4. Temperature curves for diverse magnitudes of ψ.

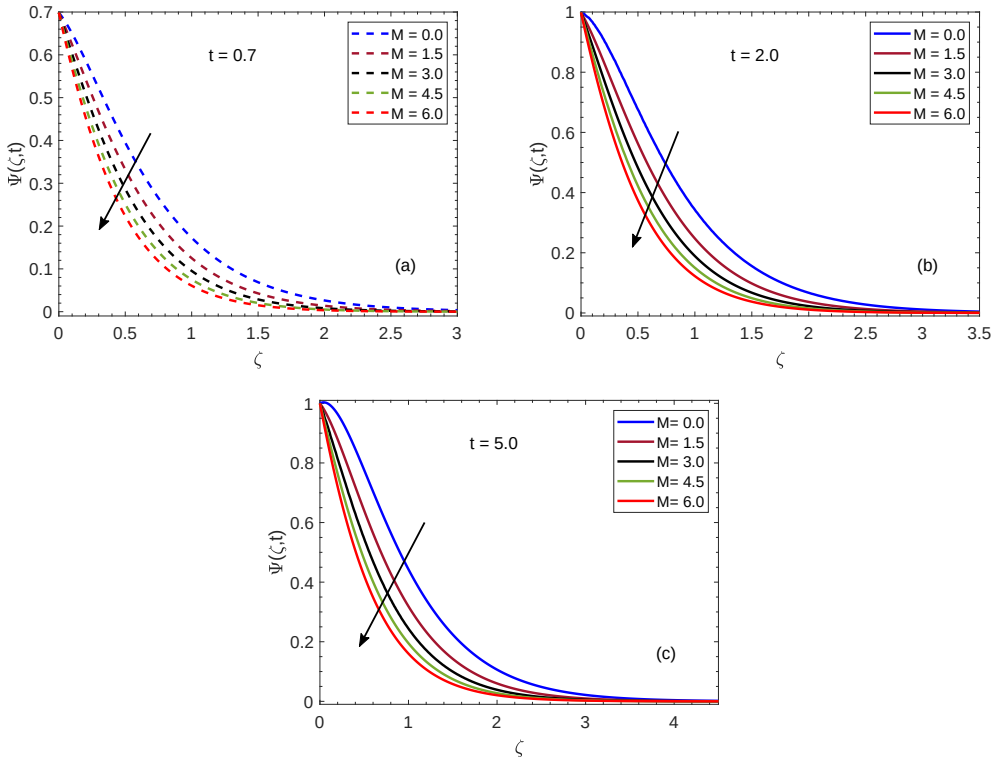

Figure 5. Flow patterns for diverse magnitudes of M.

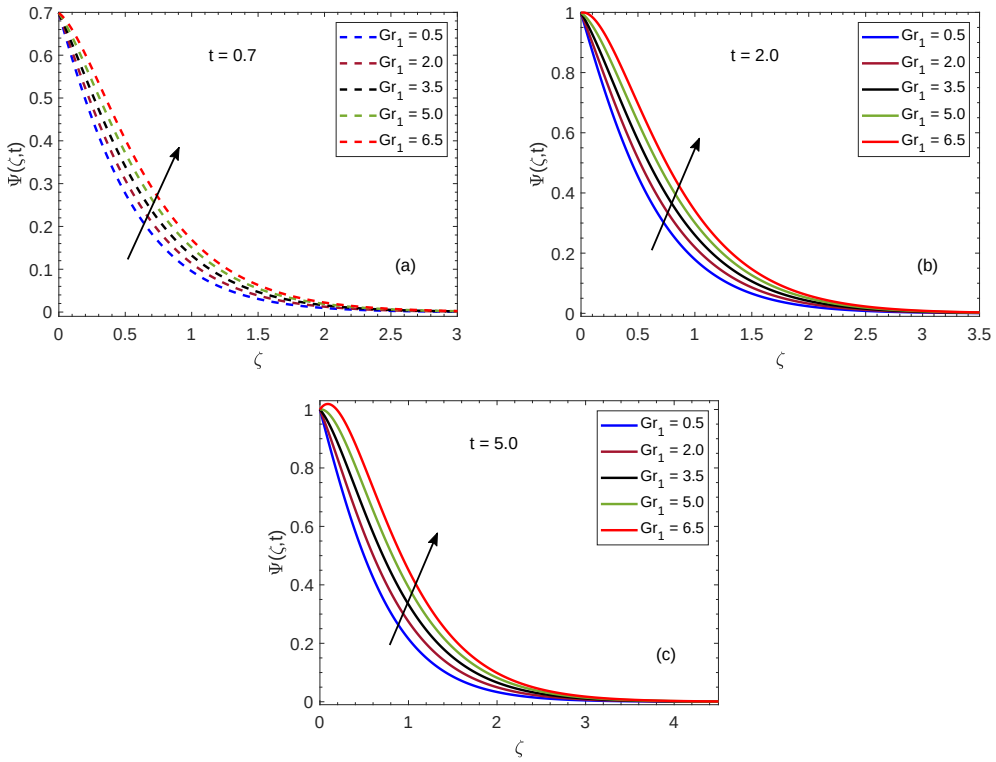

Figure 6. Flow patterns for diverse magnitudes of Gr_1.

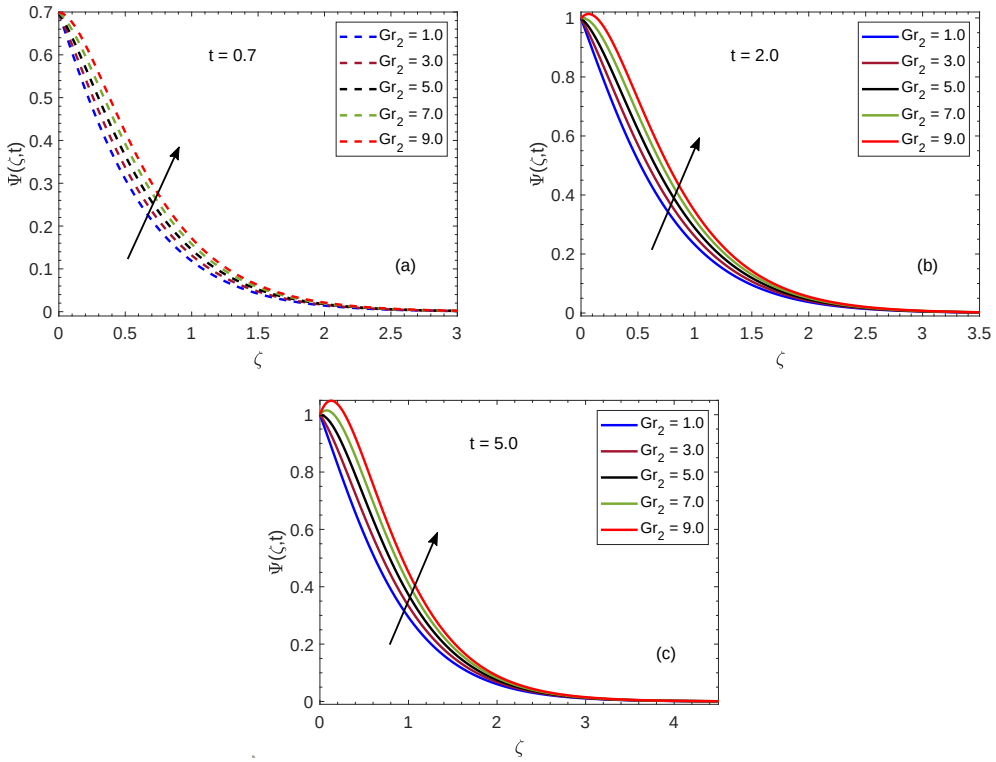

Figure 7. Flow patterns for diverse magnitudes of Gr_2.

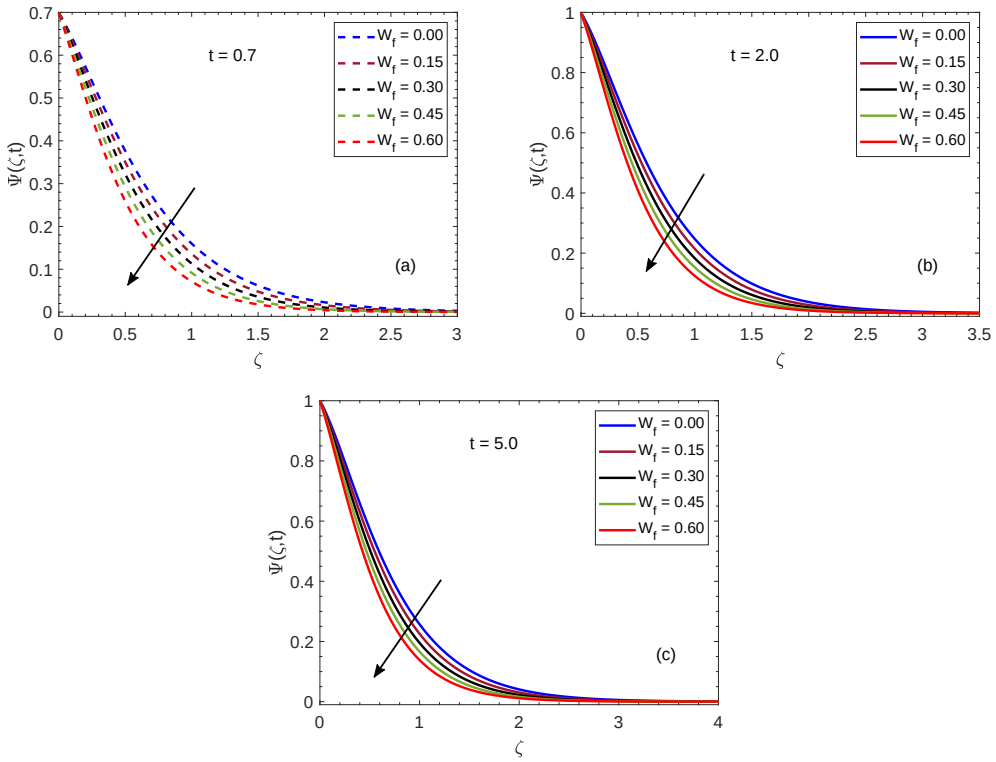

Figure 8. Flow patterns for diverse magnitudes of W_f.

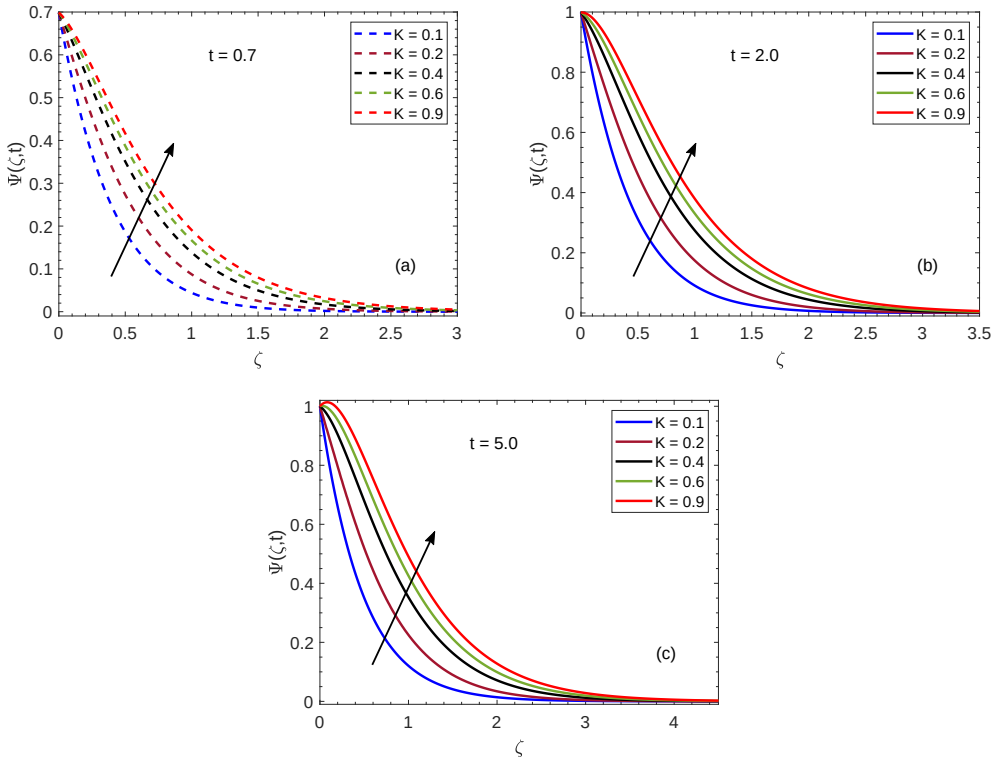

Figure 9. Flow patterns for diverse magnitudes of K.

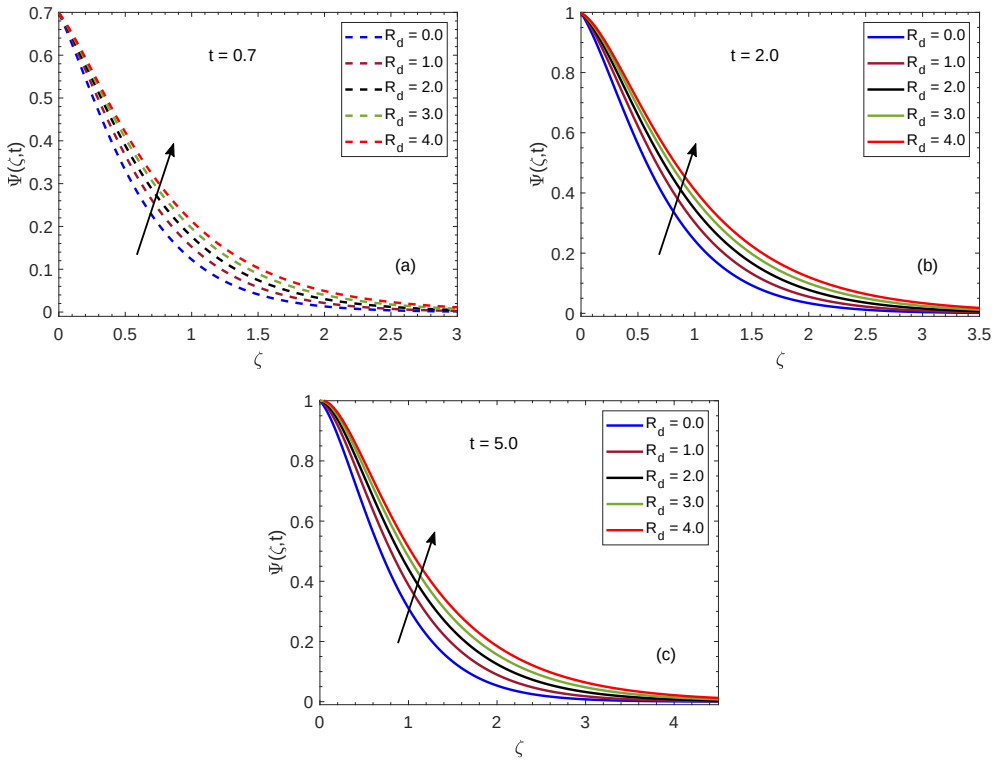

Figure 10. Flow patterns for diverse magnitudes of R_d.

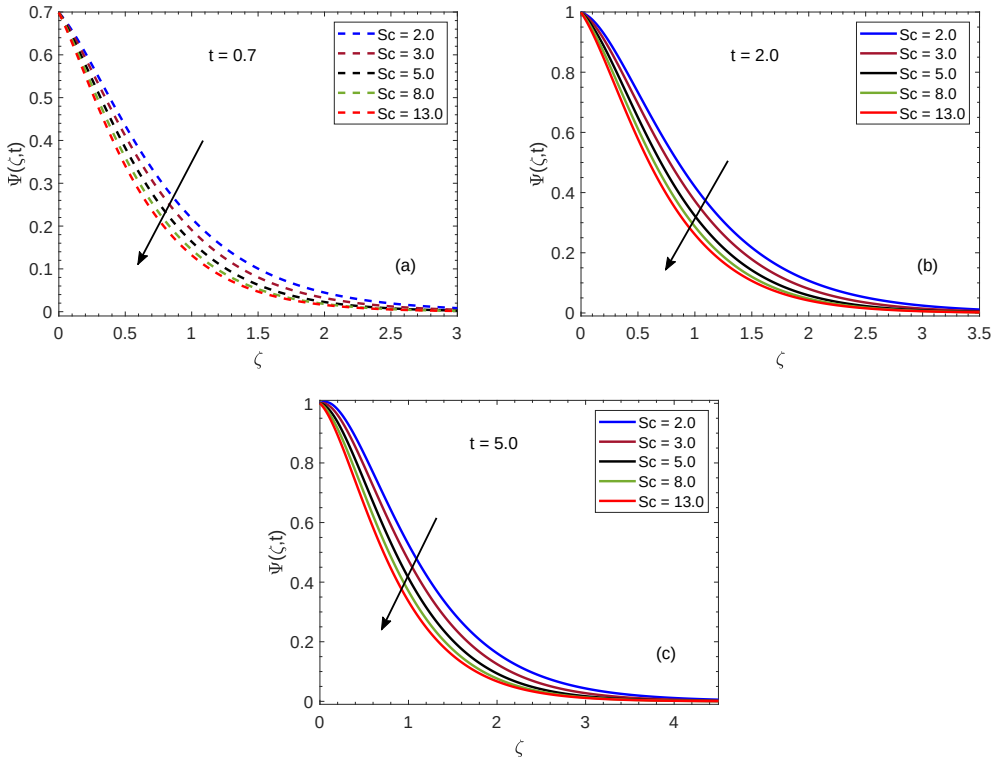

Figure 11. Flow patterns for diverse magnitudes of Sc.

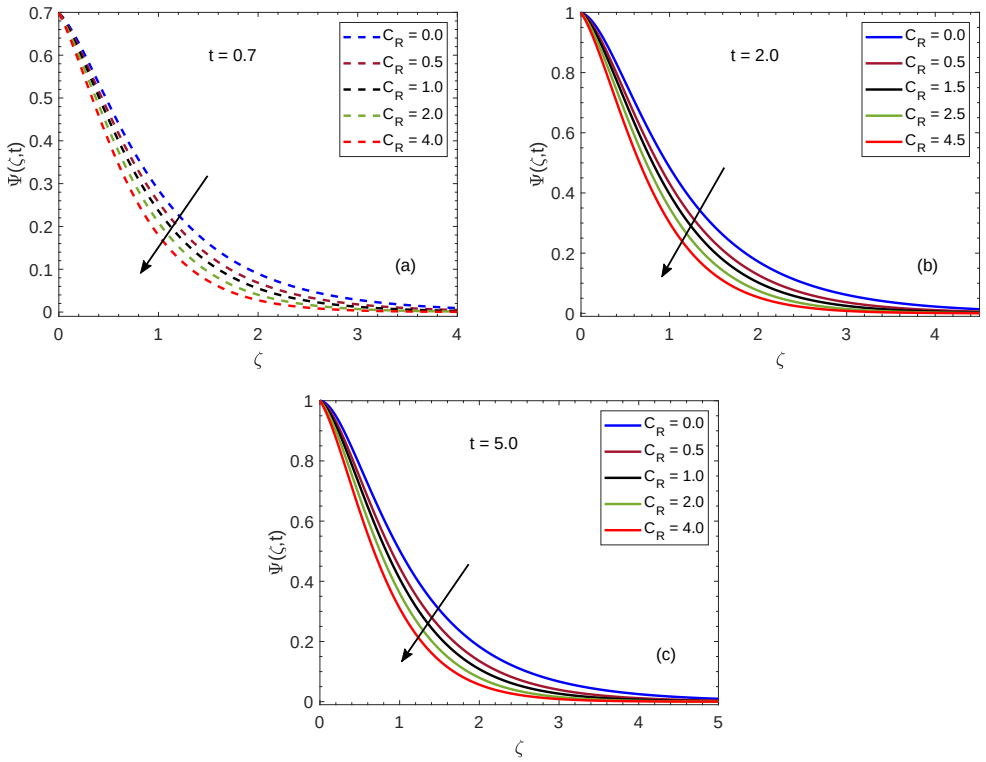

Figure 12. Flow patterns for diverse magnitudes of C_R.

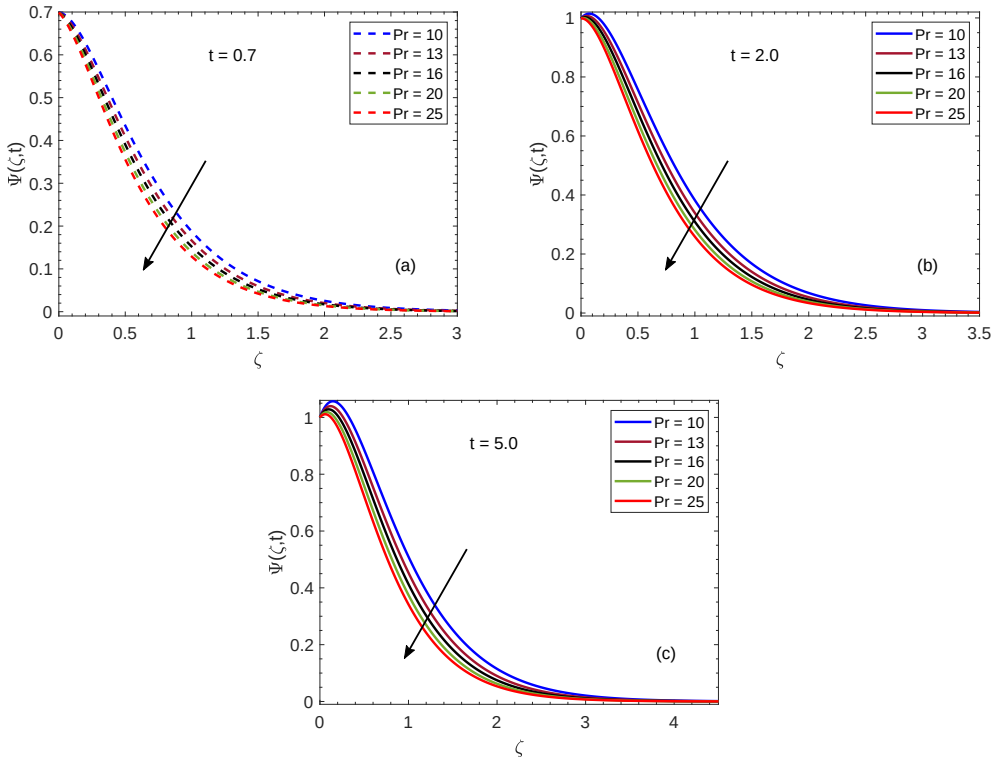

Figure 13. Flow patterns for diverse magnitudes of Pr.

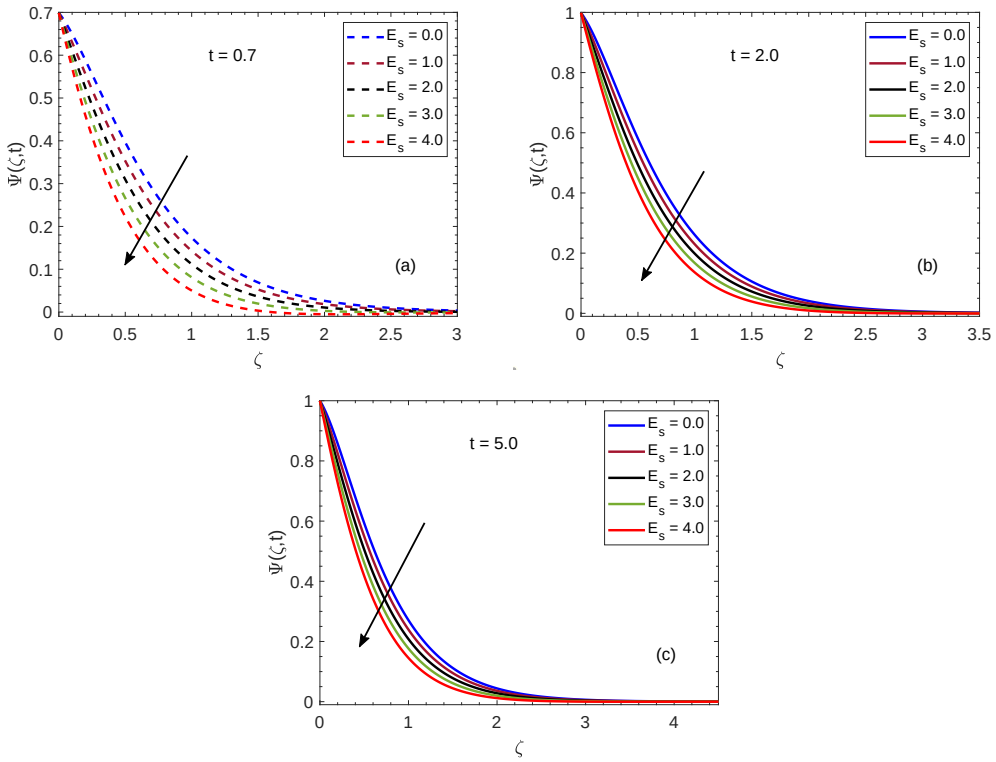

Figure 14. Flow patterns for diverse magnitudes of E_s.

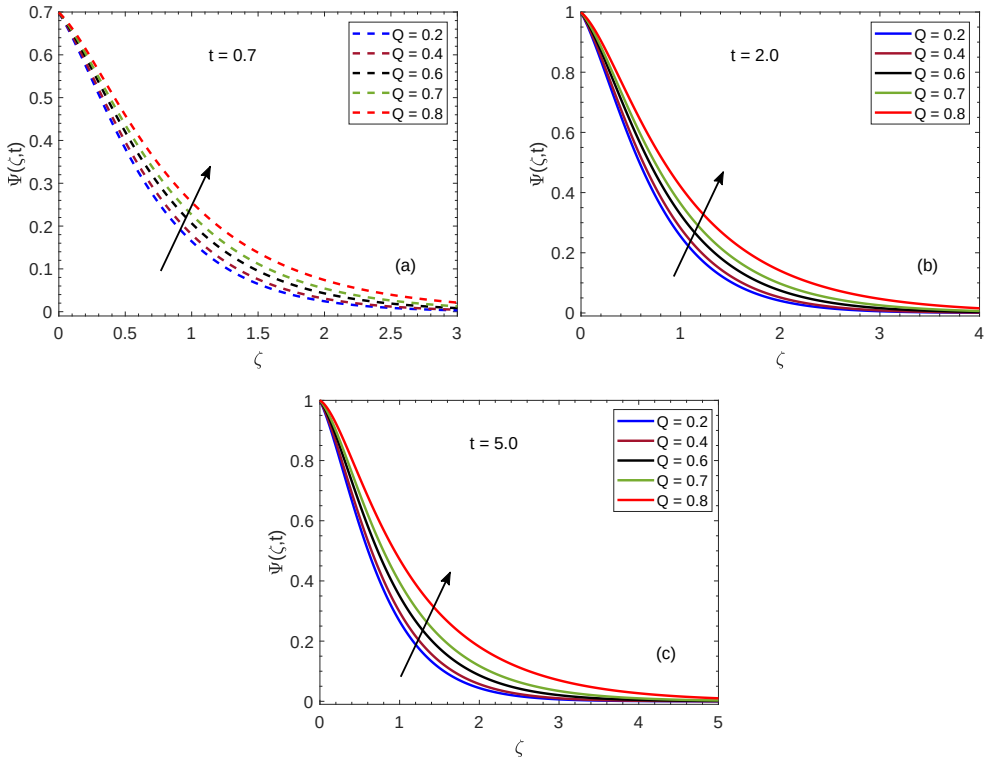

Figure 15. Flow patterns for diverse magnitudes of Q.

The computations for Nu and Sh are arranged in Tables 1 and 2 to perform a detailed numerical study about rates of heat transfer and mass transfer respectively. To clearly observe the impacts of imposed boundary conditions and fractional parameter ψ, these tables showcase the results for a wide range of values of time t and ψ. The reported results show that ψ and t offer dual nature contribution to the aforementioned processes. Precisely stating, subject to ramped conditions ($t < 1$), augmented values of ψ result in enhancement of Nu and Sh, and maximum values are obtained for integer-order expressions. Whereas, for isothermal conditions ($t > 1$), completely opposite trends are witnessed, which indicate that Nu and Sh decline for rising values of ψ. In this case, integer-order expressions produce minimum values. In a likewise manner, time advancement up to $t < 1$ augments the transfer rates, and after that, they keep reducing for $t > 1$. These results suggest that the combination of isothermal conditions with a fractional model is more efficient to attain the improved transfer rates as equated to classical model and ramped conditions. Table 3 is bestowed to perceive and interpret the variations in Sh and Nu for the physical and thermal parameters. It is noticed that the parameters C_R and Sc act in a similar fashion for Sh and diminish the mass transfer rate. Nusselt number follows inverse trends for extending domains of R_d and Pr. Extensively, Nu is a decelerating function of R_d and an escalating function of Pr. Besides this, the induction of a heat injector depreciates the Nu, whereas the existence of a heat absorbent helps to transfer the heat more swiftly. The numerical outcomes for C_f are enumerated in Tables 4 and 5 for extensive inspection of the shear stress. Shear stress is a key feature for several practical problems, and usually, boosted shear stress is seen as a leading deficiency for technical analyses. To determine an adequate solution of this drawback for the considered problem, the behavior of shear stress for several pertinent parameters is discussed with the help of Tables 4

and 5. Table 4 indicates that the use of ramped boundary condition is more suitable to control the shear stress. Moreover, it is recognized from Table 5 that dominant magnetic and electro-osmotic forces can suppress shear stress. Simultaneously, a favorable choice of the parameters Gr_1, Gr_2, and K is another effective method to serve the desired cause. Finally, it is viewed that the response of C_f under variation of ψ and t is exactly opposite to the responses of Nu and Sh. In the end, some key advantages of conducting this analysis are briefly elaborated. For instance, the current work is purely based on exact solutions and they can be utilized for verification of the several numerical techniques. Moreover, the considered problem is modeled in terms of fractional derivative, which leads to providing more general results. A suitable adjustment of the fractional parameter not only yields a perfect agreement between experimental data and theoretical outcomes but also the results for classical models can be evaluated. Several existing results can be traced through a simple modification of some parameters. Furthermore, simultaneous application of piece-wise time-dependent boundary conditions to capture flow, mass, and heat transfer dynamics through Atangana-Baleanu fractional derivative is not yet investigated. So, in this context, this study contributes to the literature extensively. However, it is also significant to discuss some limitations of this study, which will help readers to easily understand this work. Based on these limitations, this work can be modified and extended in the future. The limitations and assumptions of this work are as follows:

- The flow is incompressible, laminar, and one-dimensional.
- A linear chemical reaction is considered for the mass equation.
- Induced magnetic effects are ignored. Moreover, the influence of thermal radiation and the magnetic field is assumed negligible along the vertical axis.
- Impacts of viscous dissipation are considered insignificant for the energy equation.

Table 1. A detailed investigation of impacts of ψ and t on heat transfer rate through numerical computations.

ψ	Nusselt number					
	$t = 0.2$	$t = 0.5$	$t = 0.8$	$t = 1.4$	$t = 1.8$	$t = 2.2$
0.1	0.4950	1.2361	1.9933	2.4548	2.4329	2.4241
0.2	0.5094	1.2579	2.0159	2.4424	2.4026	2.3911
0.3	0.5324	1.2940	2.0539	2.4235	2.3530	2.3195
0.4	0.5648	1.3451	2.1076	2.3963	2.2820	2.2176
0.5	0.6083	1.4132	2.1779	2.3560	2.1844	2.0817
0.6	0.6668	1.5014	2.2651	2.2930	2.0520	1.9070
0.7	0.7474	1.6138	2.3682	2.1912	1.8743	1.6910
0.8	0.8648	1.7541	2.4803	2.0251	1.6437	1.4398
0.9	1.0486	1.9122	2.5798	1.7690	1.3747	1.1793
1.0	1.2921	2.0282	2.6228	1.4555	1.1443	0.9646

Table 2. A detailed investigation of impacts of ψ and t on mass transfer rate through numerical computations.

ψ	Sherwood number					
	$t = 0.2$	$t = 0.5$	$t = 0.8$	$t = 1.4$	$t = 1.8$	$t = 2.2$
0.1	0.6983	1.7455	2.8163	3.4733	3.4444	3.4275
0.2	0.7136	1.7687	2.8403	3.4600	3.4121	3.4018
0.3	0.7384	1.8072	2.8806	3.4392	3.3588	3.3254
0.4	0.7735	1.8621	2.9378	3.4083	3.2815	3.2160
0.5	0.8214	1.9359	3.0128	3.3613	3.1738	3.0688
0.6	0.8868	2.0322	3.1061	3.2864	3.0256	2.8783
0.7	0.9783	2.1564	3.2163	3.1640	2.8240	2.6411
0.8	1.1137	2.3123	3.3352	2.9634	2.5605	2.3652
0.9	1.3287	2.4879	3.4363	2.6541	2.2529	2.0819
1.0	1.6166	2.6107	3.4657	2.2768	1.9670	1.8313

Table 3. A detailed investigation of impacts of related parameters on Sherwood and Nusselt numbers through numerical computations.

Sherwood number			Nusselt number			
Sc	C_R	$\boldsymbol{Sh}$	R_d	Pr	Q	$\boldsymbol{Nu}$
10	0.5	2.8887	1.0	10	0.1	1.6471
-	1.5	3.6358	2.0	-	-	1.3449
-	2.5	4.2542	3.0	-	-	1.1647
2.0	-	1.1734	0.5	10	-	1.9019
3.0	-	1.4371	-	15	-	2.3294
5.0	-	1.8553	-	20	-	2.6897
			-	10	−0.2	2.1423
			-	-	−0.4	2.2887
			-	-	0.0	1.9852
			-	-	0.2	1.8149
			-	-	0.4	1.6273

Table 4. A detailed investigation of impacts of ψ and t on shear stress through numerical computations.

ψ	Skin friction coefficient					
	$t = 0.2$	$t = 0.5$	$t = 0.8$	$t = 1.4$	$t = 1.8$	$t = 2.2$
0.1	−0.2298	−0.3910	−0.5550	−0.6510	−0.6441	−0.6433
0.2	−0.2373	−0.4030	−0.5677	−0.6446	−0.6280	−0.6199
0.3	−0.2493	−0.4226	−0.5887	−0.6351	−0.6016	−0.5813
0.4	−0.2658	−0.4500	−0.6184	−0.6225	−0.5649	−0.5270
0.5	−0.2873	−0.4861	−0.6571	−0.6050	−0.5157	−0.4554
0.6	−0.3151	−0.5321	−0.7052	−0.5794	−0.4509	−0.3646
0.7	−0.3519	−0.5897	−0.7627	−0.5393	−0.3664	−0.2531
0.8	−0.4032	−0.6611	−0.8274	−0.4745	−0.2580	−0.1220
0.9	−0.4810	−0.7444	−0.8920	−0.3744	−0.1292	0.0203
1.0	−0.5824	−0.8126	−0.9370	−0.2592	−0.0117	0.1476

Table 5. A detailed investigation of impacts of related parameters on shear stress through numerical computations.

Skin friction coefficient						
Gr_1	Gr_2	M	E_s	W_f	K	C_f
2.0	4.0	1.0	0.5	0.1	0.4	−0.8796
3.0	-	-	-	-	-	−0.7378
5.0	-	-	-	-	-	−0.4539
4.0	3.0	-	-	-	-	−0.7132
-	5.0	-	-	-	-	−0.4785
-	7.0	-	-	-	-	−0.2439
-	4.0	1.5	-	-	-	−0.6916
-	-	3.0	-	-	-	−0.9510
-	-	4.5	-	-	-	−1.1790
-	-	1.0	2.0	-	-	−0.9590
-	-	-	3.0	-	-	−1.2013
-	-	-	4.0	-	-	−1.4436
-	-	-	0.5	0.1	-	−0.5841
-	-	-	-	0.2	-	−0.5613
-	-	-	-	0.3	-	−0.5277
-	-	-	-	0.1	0.2	−1.0347
-	-	-	-	-	0.4	−0.5958
-	-	-	-	-	0.6	−0.4202

5. Summary and conclusions

The core motive of this research piece is to examine the influence of electro-osmotic forces on MHD fractional flow of a Walters' B fluid close to a vertical wall nested in a porous material. Besides this, mass transfer rate and radiative thermal performance are analyzed subject to ramped concentration and energy of the bounding wall. The impacts of first-order chemical reaction and heat injection/absorption are also evaluated in this work. A time-controlled velocity condition is imposed, which leads to develop the flow of the considered fluid. The unit-less conventional equations of the considered problem are generalized to the fractional form operating the non-singular and non-local

kernel-based Atangana-Baleanu derivative. The consequent equations are solved analytically, and exact solutions are determined by exercising the Laplace transform technique. To analyze the features of influential parameters, effects of generalizing the model, and advantages of using the ramped surface conditions, a comprehensive tabular and graphical study is performed. The extracted key results of the current work are summarized as

- The velocity of flow drops due to extension in the domain of the parameter E_s. This behavior of the velocity profile has exceptional applications in minimizing the deterioration and dampness of wall structures [52]. At the atomic level, the electro-osmosis phenomenon is also used in fluids' separation processes, which can be efficiently utilized as medication dischargers [54].
- Heat and mass transfer rates reveal interesting features for variation in ψ and t. More specifically, for $t < 1$, an escalation in ψ and t enhances the observed rates. Later, for $t > 1$, mass and heat transfer rates act in a reverse fashion and show decreasing behavior for an upsurge in t and ψ.
- Application of the ramping strategy on the bounding wall is more efficient when augmentation of the heat transfer rate and reduction of shear stress are the primary goals.
- The fractional parameter ψ specifies a dual role for ramped and isothermal conditions. Precisely, for $t < 1$, it declines the velocity, concentration, and energy profiles, but for $t > 1$, these quantities keep increasing as a result of a rise in ψ.
- For $t < 1$, the fundamental functions involved in this study are maximum for the fractional model, whereas, for $t > 1$, the classical model provides the highest profiles of these functions.
- Electro-osmotic and magnetic effects cause to reduce the shear stress at the bounding wall.
- The comparative analysis of solutions for isothermal and ramped conditions indicate that curves representing concentration, velocity, and energy functions are higher for isothermal conditions.
- Time-controlled boundary conditions possess vital significance in order to gain the swiftest cooling rate and improved flow control.

Acknowledgments

The authors acknowledge the financial support provided by the Center of Excellence in Theoretical and Computational Science (TaCS-CoE), KMUTT. Moreover, this research project is supported by Thailand Science Research and Innovation (TSRI) Basic Research Fund: Fiscal year 2021 under project number 64A306000005. The first and third authors appreciate the support provided by Petchra Pra Jom Klao Ph.D. Research Scholarship (Grant No. 25/2563 and 14/2562).

Conflict of interest

The authors declare no conflict of interest.

References

1. F. F. Reuss, Charge-induced flow, *Proc. Imp. Soc. Nat. Moscow*, **3** (1809), 327–344.
2. G. Wiedemann, Ueber die Bewegung von Flüssigkeiten im Kreise der geschlossenen galvanischen Säule, *Ann. Phys.*, **163** (1852), 321–352.

3. M. V. Smoluchowski, Elektrische endosmose und stromungsstrome, *Handbuch del Elektrizitat und des Magnetismus*, **2** (1921), 366.
4. D. H. Gray, Electrochemical hardening of clay soils, *Geotechnique*, **20** (1970), 81–93.
5. A. Asadi, B. B. Huat, H. Nahazanan, H. A. Keykhah, Theory of electroosmosis in soil, *Int. J. Electrochem. Sci.*, **8** (2013), 1016–1025.
6. V. Chokkalingam, B. Weidenhof, M. Krämer, W. F. Maier, S. Herminghaus, R. Seemann, Optimized droplet-based microfluidics scheme for sol–gel reactions, *Lab Chip*, **10** (2010), 1700–1705.
7. A. Manz, C. S. Effenhauser, N. Burggraf, D. J. Harrison, K. Seiler, K. Fluri, Electroosmotic pumping and electrophoretic separations for miniaturized chemical analysis systems, *J. Micromech. Microeng.*, **4** (1994), 257.
8. S. Deng, The parametric study of electroosmotically driven flow of power-law fluid in a cylindrical microcapillary at high zeta potential, *Micromachines*, **8** (2017), 344.
9. S. Sarkar, P. M. Raj, S. Chakraborty, P. Dutta, Three-dimensional computational modeling of momentum, heat, and mass transfer in a laser surface alloying process, *Numer. Heat Transfer A*, **42** (2002), 307–326.
10. Y. Hu, C. Werner, D. Li, Electrokinetic transport through rough microchannels, *Anal. Chem.*, **75** (2003), 5747–5758.
11. G. H. Tang, X. F. Li, Y. L. He, W. Q. Tao, Electroosmotic flow of non-Newtonian fluid in microchannels, *J. non-Newton. Fluid Mech.*, **157** (2009), 133–137.
12. Q. Liu, Y. Jian, L. Yang, Alternating current electroosmotic flow of the Jeffreys fluids through a slit microchannel, *Phys. Fluids*, **23** (2011), 102001.
13. C. Zhao, E. Zholkovskij, J. H. Masliyah, C. Yang, Analysis of electroosmotic flow of power-law fluids in a slit microchannel, *J. Colloid Interf. Sci.*, **326** (2008), 503–510.
14. Q. S. Liu, Y. J. Jian, L. G. Yang, Time periodic electroosmotic flow of the generalized Maxwell fluids between two micro-parallel plates, *J non-Newton. Fluid Mech.*, **166** (2011), 478–486.
15. C. Zhao, C. Yang, Joule heating induced heat transfer for electroosmotic flow of power-law fluids in a microcapillary, *Int. J. Heat Mass Tran.*, **55** (2012), 2044–2051.
16. A. Bandopadhyay, D. Tripathi, S. Chakraborty, Electroosmosis-modulated peristaltic transport in microfluidic channels, *Phys. Fluids*, **28** (2016), 052002.
17. S. S. Hsieh, H. C. Lin, C. Y. Lin, Electroosmotic flow velocity measurements in a square microchannel, *Colloid Polym. Sci.*, **284** (2006), 1275–1286.
18. S. Hadian, S. Movahed, N. Mokhtarian, Analytical study of temperature distribution of the electroosmotic flow in slit microchannels, *World Appl. Sci. J.*, **17** (2012), 666–671.
19. M. Dejam, Derivation of dispersion coefficient in an electro-osmotic flow of a viscoelastic fluid through a porous-walled microchannel, *Chem. Eng. Sci.*, **204** (2019), 298–309.
20. J. C. Misra, A. Sinha, Electro-osmotic flow and heat transfer of a non-Newtonian fluid in a hydrophobic microchannel with Navier slip, *J. Hydrodynam. Ser. B*, **27** (2015), 647–657.

21. R. Ponalagusamy, R. Manchi, Particle-fluid two phase modeling of electro-magneto hydrodynamic pulsatile flow of Jeffrey fluid in a constricted tube under periodic body acceleration, *Eur. J. Mech. B Fluid.*, **81** (2020), 76–92.
22. M. Azari, A. Sadeghi, S. Chakraborty, Electroosmotic flow and heat transfer in a heterogeneous circular microchannel, *Appl. Math. Model.*, **87** (2020), 640–654.
23. M. Dejam, Hydrodynamic dispersion due to a variety of flow velocity profiles in a porous-walled microfluidic channel, *Int. J. Heat Mass Tran.*, **136** (2019), 87–98.
24. A. J. Moghadam, Heat transfer in electrokinetic micro-pumps under the influence of various oscillatory excitations, *Eur. J. Mech. B Fluid.*, **85** (2020), 158–168.
25. T. Alqahtani, S, Mellouli, A. Bamasag, F. Askri, P. E. Phelan, Thermal performance analysis of a metal hydride reactor encircled by a phase change material sandwich bed, *Int. J. Hydrog. Energy*, **45** (2020), 23076–23092.
26. U. Khan, A. Zaib, D. Baleanu, M. Sheikholeslami, A. Wakif, Exploration of dual solutions for an enhanced cross liquid flow past a moving wedge under the significant impacts of activation energy and chemical reaction, *Heliyon*, **6** (2020), e04565.
27. H. R. Kataria, H. R. Patel, Effects of chemical reaction and heat generation/absorption on magnetohydrodynamic (MHD) casson fluid flow over an exponentially accelerated vertical plate embedded in porous medium with ramped wall temperature and ramped surface concentration, *Propuls. Power Res.*, **8** (2019), 35–46.
28. J. Zhao, Thermophoresis and Brownian motion effects on natural convection heat and mass transfer of fractional Oldroyd-B nanofluid, *Int. J. Fluid Mech. Res.*, **47** (2020), 357–370.
29. P. K. Gaur, R. P. Sharma, A. K. Jha, Transient free convective radiative flow between vertical parallel plates heated/cooled asymmetrically with heat generation and slip condition, *Int. J. Appl. Mech. Eng.*, **23** (2018), 365–384.
30. L. Wang, D. W. Sun, Recent developments in numerical modelling of heating and cooling processes in the food industry–a review, *Trends Food Sci. Tech.*, **14** (2003), 408–423.
31. S. Islam, A. Khan, P. Kumam, H. Alrabaiah, Z. Shah, W. Khan, et al., Radiative mixed convection flow of Maxwell nanofluid over a stretching cylinder with Joule heating and heat source/sink effects, *Sci. Rep.*, **10** (2020), 17823.
32. A. Baslem, G. Sowmya, B. J. Gireesha, B. C. Prasannakumara, M. R. Gorji, N. M. Hoang, Analysis of thermal behavior of a porous fin fully wetted with nanofluids: convection and radiation, *J. Mol. Liq.*, **307** (2020), 112920.
33. T. Hayat, M. W. A. Khan, M. I. Khan, A. Alsaedi, Nonlinear radiative heat flux and heat source/sink on entropy generation minimization rate, *Physica B*, **538** (2018), 95–103.
34. C. Sulochana, G. P. Ashwinkumar, N. Sandeep, Effect of frictional heating on mixed convection flow of chemically reacting radiative Casson nanofluid over an inclined porous plate, *Alex. Eng. J.*, **57** (2018), 2573–2584.
35. K. S. Miller, B. Ross, *An introduction to the fractional calculus and fractional differential equations*, Wiley, 1993.

36. S. Das, T. Das, S. Chakraborty, Analytical solutions for the rate of DNA hybridization in a microchannel in the presence of pressure-driven and electroosmotic flows, *Sensors Actuat. B Chem.*, **114** (2006), 957–963.
37. S. Das, S. Chakraborty, Transverse electrodes for improved DNA hybridization in microchannels, AIChE J., **53** (2007), 1086–1099.
38. D. Kumar, J. Singh, M. A. Qurashi, D. Baleanu, A new fractional SIRS-SI malaria disease model with application of vaccines, antimalarial drugs, and spraying, *Adv. Differ. Equ.*, **2019** (2019), 278.
39. I. Ahmed, I. A. Baba, A. Yusuf, P. Kumam, W. Kumam, Analysis of Caputo fractional-order model for COVID-19 with lockdown, *Adv. Differ. Equ.*, **2020** (2020), 1–14.
40. S. Ullah, M. A. Khan, J. F. G. Aguilar, Mathematical formulation of hepatitis B virus with optimal control analysis, *Optim. Contr. Appl. Meth.*, **40** (2019), 529–544.
41. B. Acay, E. Bas, T. Abdeljawad, Fractional economic models based on market equilibrium in the frame of different type kernels, *Chaos Soliton. Fract.*, **130** (2020), 109438.
42. A. Kilbas, H. Srivastava, J. Trujillo, *Theory and applications of fractional differential equations*, Elsevier, 2006.
43. I. Podlubny, *Fractional differential equations: An introduction to fractional derivatives, fractional differential equations, to methods of their solution and some of their applications*, Amsterdam, The Netherlands: Elsevier, 1998.
44. M. Caputo, M. Fabrizio, A new definition of fractional derivative without singular kernel, *Progr. Fract. Differ. Appl.*, **1** (2015), 1–13.
45. A. Atangana, D. Baleanu, New fractional derivatives with nonlocal and non-singular kernel: Theory and application to heat transfer model, *Therm. Sci.*, **4** (2016), 763–769.
46. A. Gemant, XLV. On fractional differentials, *The London, Edinburgh, and Dublin Philosophical Magazine and Journal of Science*, **25** (1938), 540–549.
47. S. Aman, Q. A. Mdallal, I. Khan, Heat transfer and second order slip effect on MHD flow of fractional Maxwell fluid in a porous medium, *J. King Saud Univ. Sci.*, **32** (2020), 450–458.
48. A. Awan, M. D. Hisham, N. Raza, The effect of slip on electro-osmotic flow of a second-grade fluid between two plates with Caputo–Fabrizio time fractional derivatives, *Can. J. Phys.*, **97** (2019), 509–516.
49. Y. Jiang, H. Qi, H. Xu, X. Jiang, Transient electroosmotic slip flow of fractional Oldroyd-B fluids, *Microfluid. Nanofluid.*, **21** (2017), 7.
50. M. I. Asjad, M. Aleem, A. Ahmadian, S. Salahshour, M. Ferrara, New trends of fractional modeling and heat and mass transfer investigation of (SWCNTs and MWCNTs)-CMC based nanofluids flow over inclined plate with generalized boundary conditions, *Chin. J. Phys.*, **66** (2020), 497–516.
51. C. Bardos, F. Golse, B. Perthame, The Rosseland approximation for the radiative transfer equations, *Commun. Pure Appl. Math.*, **40** (1987), 691–721.
52. L. M. Ottosen, A. J. Pedersen, I. R. Dalgaard, Salt-related problems in brick masonry and electrokinetic removal of salts, *J. Building Appraisal*, **3** (2007), 181–194.

53. S. Chakraborty, Towards a generalized representation of surface effects on pressure-driven liquid flow in microchannels, *Appl. Phys. Lett.*, **90** (2007), 034108.

54. H. M. Park, W. M. Lee, Effect of viscoelasticity on the flow pattern and the volumetric flow rate in electroosmotic flows through a microchannel, *Lab Chip*, **8** (2008), 1163–1170.

55. K. R. Rajagopal, M. Ruzicka, A. R. Srinivasa, On the Oberbeck-Boussinesq approximation, *Math. Mod. Meth. Appl. Sci.*, **6** (1996), 1157–1167.

56. I. Khan, F. Ali, N. A. Shah, Interaction of magnetic field with heat and mass transfer in free convection flow of a Walters'-B fluid, *Eur. Phys. J. Plus*, **131** (2016), 77.

57. F. Ali, M. Iftikhar, I. Khan, N. A. Sheikh, Aamina, K. S. Nisar, Time fractional analysis of electro-osmotic flow of Walters's-B fluid with time-dependent temperature and concentration, *Alex. Eng. J.*, **59** (2020), 25–38.

58. F. Ali, M. Saqib, I. Khan, N. A. Sheikh, Application of Caputo-Fabrizio derivatives to MHD free convection flow of generalized Walters'-B fluid model, *Eur. Phys. J. Plus*, **131** (2016), 377.

Appendix

The velocity vector for the problem under observation is described as

$$\vec{q} = [u'(y', t'), 0, 0].$$

The momentum equation under Boussinesq's approximation [55] is developed as [56, 57]

$$\rho\frac{d\vec{q}}{dt'} = \vec{R} + \nabla\cdot\boldsymbol{T} + \rho g\left\{\beta_1(\Theta' - \Theta'_\infty) + \beta_2(\Phi' - \Phi'_\infty)\right\} + \vec{J}\times\vec{M} + \vec{E_x}\rho_e,$$

where $\vec{J}\times\vec{M}$ is the product of current density and net magnetic field, $\vec{E_x}$ deals with the externally imposed electric field, β_1 and β_2 are the thermal and mass expansion coefficients respectively, $\vec{R}$ shows the force of porous medium's resistance, and ρ_e specifies the total electric charge density. The terms ρ_e and $\boldsymbol{T}$ are described as [57]

$$\rho_e = -\epsilon\kappa_e^2\psi_w\exp\left(-\kappa_e y'\right), \quad \boldsymbol{T} = \mu\boldsymbol{B_1} + \kappa_1\boldsymbol{B_1}^2 - \kappa_0\boldsymbol{B_2} - p\boldsymbol{I}.$$

Here, the kinematic tensors $\boldsymbol{B_1}$ and $\boldsymbol{B_2}$ are defined as [58]

$$\boldsymbol{B_1} = \nabla\vec{q} + (\nabla\vec{q})^T, \quad \boldsymbol{B_2} = \boldsymbol{B_1}(\nabla\vec{q}) + \boldsymbol{B_1}(\nabla\vec{q})^T + \frac{d\boldsymbol{B_1}}{dt'}.$$

Some of the terms in flow equation have the following form

$$\frac{d\vec{q}}{dt'} = \frac{\partial u'}{\partial t'},$$
$$\vec{J} \times \vec{M} = -\sigma M_0^2 u',$$
$$\vec{R} = \frac{\varphi}{\alpha_0}\left(\mu - \kappa_0 \frac{\partial}{\partial t'}\right) u',$$
$$\nabla \cdot \boldsymbol{T} = \left(\mu - \kappa_0 \frac{\partial}{\partial t'}\right) \frac{\partial^2 u'}{\partial y'^2}.$$